THE ASTROPHYSICAL JOURNAL, 361:78–97, 1990 September 20

VELOCITY MAPPING AND MODELS OF THE ELLIPTICAL GALAXIES NGC 720, NGC 1052, AND NGC 4697

J. J. BINNEY
Steward Observatory and Department of Theoretical Physics, Oxford University
ROGER L. DAVIES[1]
National Optical Astronomical Observatories[2] and Department of Astrophysics, Oxford University
AND
GARTH D. ILLINGWORTH[1]
University of California Observatories/Lick Observatory and the Board of Studies in Astronomy and Astrophysics, University of California, Santa Cruz
Received 1989 March 15; accepted 1990 March 20

ABSTRACT

Extensive long-slit spectroscopic observations of the E3–E4 elliptical galaxies NGC 720, 1052, and 4697 are presented, including results from slits that are parallel to the major and minor axes but which do not pass through the nucleus. A novel deprojection algorithm is used to construct axisymmetric mass models of these systems from CCD surface photometry. These mass models are combined with the Jeans equations to yield predicted fields of line-of-sight velocity dispersion and streaming velocity. Comparison of these fields with the observed velocities imply: (i) none of these systems can have isotropic velocity dispersion tensors; (ii) diminishing the assumed inclination i of any given galaxy tends to decrease the line-of-sight velocity dispersion and, counterintuitively, to increase the line-of-sight rotation speeds; (iii) the ratio of the line-of-sight velocity dispersion along the minor axis to that along the major axis is a sensitive diagnostic of the importance of a third integral for a galaxy's structure; (iv) our observations of NGC 1052 can be successfully modeled with a distribution function of the form $f(E, L_z)$ but our observations of NGC 720 and NGC 4697 cannot; (v) in NGC 4697 the observed rotation speeds tend to decline away from the major axis faster than the models predict; and (vi) the data are consistent with constant mass-to-light ratio through the studied portions of all three systems.

Subject headings: galaxies: formation — galaxies: individual (NGC 720, 1052, 4697) — galaxies: internal motions — galaxies: structure

I. INTRODUCTION

Elliptical galaxies should be the simplest galaxies since they are dominated by a single hot component. Hence, it is natural to construct dynamical models of such systems and to compare the predictions of those models with the extensive observations of elliptical galaxies that have been made in the last decade.

Early work concentrated on modeling apparently round galaxies, with particular emphasis on whether such systems could have constant mass-to-light ratios Υ, particularly in their nuclei and at large radii. Either a central black hole (Sargent *et al.* 1978) or a dark halo (Dressler 1979; Efstathiou, Ellis, and Carter 1982) should be detectable through radial gradients in the measured Υ. Two important observational limitations on such studies are (i) the difficulty of achieving high spatial resolution in ground-based velocity dispersion and photometric measurements and (ii) the difficulty of measuring the dispersion far enough from the centers to demonstrate that Υ rises at large r. The observational uncertainties introduced by these difficulties have so far permitted us to build equilibrium (but possibly unstable; Merritt 1987) models of giants such as M87 with constant Υ (see e.g., Binney and Petit 1988 for a review). However, a crucial element in successfully modeling a spherical galaxy with constant Υ is the freedom to adjust the relative importance of tangential and radial motions in the model (Binney and Mamon 1982; Tonry 1983).

Two-dimensional observations of an axisymmetric galaxy clearly contain more independent data points than comparable observations of a spherical system, and one might hope that the allowed models would be correspondingly more tightly constrained. Indeed, the most convincing evidence for a central black hole comes from the flattened, spinning dwarf elliptical M32 (Tonry 1984; Dressler and Richstone 1988). Hence, one motivation for undertaking the work reported here was to learn what light can be shed on these questions by examining the velocity fields of flattened galaxies in full two-dimensional detail. A further example of the value of such studies comes from Fillmore (1986), who notes that the ratio of the minor to the major axis velocity dispersions is a key diagnostic of the velocity ellipsoid structure.

Prendergast and Tomer (1970) and then Wilson (1975) made the first concerted attempts to model rotating elliptical galaxies. These authors developed techniques for constructing flattened systems with distribution functions of the form $f(E, L_z)$, where E and L_z are, respectively, the energy and angular momentum of an individual star about the galaxy's symmetry axis. This early work ran into two problems. First, with distribution functions of the form then employed, all models became rather spherical (or even prolate!) and slowly rotating away from the core, and, second, the peak rotation speeds

[1] Visiting Astronomer at the Kitt Peak National Observatory and the Cerro Tololo Inter-American Observatory, operated by AURA, Inc., under contract to the National Science Foundation.
[2] NOAO is operated by AURA, Inc., for the National Science Foundation.

required to flatten the galaxies adequately were larger than the observations allowed. However, Jarvis and Freeman (1985) and Rowley (1988) showed that the techniques developed in the early studies, while inappropriate for ellipticals, could be exploited to produce models of the flattened bulges of disk systems that fit the observational data (Kormendy and Illingworth 1983) extremely well.

The discrepancy between the peak rotation rates predicted by the early models of elliptical galaxies and observations led to speculation that the distribution functions of elliptical galaxies (Illingworth 1977; Binney 1978), like that of the Milky Way, must depend on a third integral I_3 in addition to E and L_z. Satoh (1980) devised an elegant model to show that this implication did not follow from the data then available. Satoh introduced a two-parameter family of flattened density distributions for every member of which it is possible to integrate analytically the Jeans equations. Thus, one could obtain the mean-square values of the velocities that would be required if the system's distribution function were of the form $f(E, L_z)$. Satoh did not actually recover f, but one knows from the work of Lynden-Bell (1962), Hunter (1975), Dejonghe (1986) and Newton (1986) that $f(E, L_z)$ can, in principle, be recovered for models such as those of Satoh.

In this paper we use an extension of Satoh's technique to construct detailed models of three elliptical galaxies, NGC 720, 1052, and 4697, for which CCD surface photometry and extensive long-slit spectroscopy are available. Our work differs from that of Satoh in that we do not fit each galaxy's density profile to a few-parameter family of models, but employ a novel technique to fit the surface photometry with three-dimensional models in which the density at every point in the meridional (R, z) plane can be independently varied. We use these models and the Jeans equations with some assumed mass-to-light ratio to predict velocity dispersions and streaming velocities along each of the lines for which we have a long-slit spectrum. Thus, we probe whether it is possible to account for the observed kinematics of these galaxies under the assumptions of (i) constant mass-to-light ratio, (ii) axisymmetry, and (iii) $f = f(E, L_z)$. We show that these assumptions are viable in the case of NGC 1052, but unacceptable in the cases of NGC 4697 and NGC 720, the failure being particularly clear-cut in the last case.

The paper is organized as follows: § II describes the observational data employed, § III describes the technique used to predict kinematics from the photometry, § IV compares the true and predicted kinematics of each galaxy, and § V gives a summary. An appendix contains various formulae involved in our technique for the generation of three dimensional models from surface photometry. We give the tabulated kinematic data in a second appendix.

II. OBSERVATIONS, DATA, AND RESULTS

The three galaxies studied here, NGC 720, 1052, and 4697, are prototypical E3–E4 ellipticals. Some basic properties are given in Table 1. NGC 4697 was one of the first ellipticals for which stellar kinematical data were obtained (Bertola and Capaccioli 1975; Illingworth 1977), showing that all was not well with models of hot stellar systems (Binney 1976). It was also one of the first ellipticals in which a weak stellar disk was detected (Carter 1987; Jedrzejewski, Davies, and Illingworth 1987). NGC 1052 has long been of interest because of its central radio source and emission-line nucleus. It has been mapped in H I and has optical emission throughout the body of the galaxy (see Davies and Illingworth 1986 for references). Some dust is present in the inner regions. Davies and Illingworth suggest that its stellar and gaseous kinematical properties together indicate that NGC 1052 is probably triaxial. NGC 720 is an unusually isolated elliptical galaxy (see e.g., Dressler, Schechter, and Rose 1986). It has a surprisingly large core radius, $r_c \approx 4''$ (Jedrzejewski, Davies, and Illingworth 1987) and has also been the subject of a kinematical study of its dwarf companions. This study suggested that its overall mass-to-light ratio interior to a radius of $\approx 20'$ is some 40 times *larger* than that which would be derived at radii comparable to r_e (Dressler, Schechter, and Rose 1986). Both NGC 1052 and NGC 4697 are strong 100 μm *IRAS* sources (1400 and 1100 mJy, respectively; Knapp *et al.* 1988), while NGC 720 and NGC 4697 are X-ray sources with fluxes log L_X of 41.1 and 40.3 ergs s^{-1}, respectively (Canizares, Fabbiano, and Trinchieri 1987).

a) Surface Photometry

The R-band data used here are taken from the work of Davis *et al.* (1985), Jedrzejewski, Davies, and Illingworth (1987), and Peletier *et al.* (1990). The observing procedures and reduction and calibration techniques are described in these papers. A two-dimensional description of the surface brightness distribution is required for input into the models rather than a single azimuthally-averaged major-axis luminosity profile. Seven luminosity profiles each representing a cut through the galaxy center were generated from the galaxy images; interfering images were identified and their effects were removed as described in the above papers. These cuts were made on the

TABLE 1

PROPERTIES OF THE GALAXIES

	CLASSIFICATION							
GALAXY	RC2	RSA	B_T	r_e	ϵ	v_{grp}	D (Mpc)	M_B
(1)	(2)	(3)	(4)	(5)	(6)	(7)	(8)	(9)
NGC 720.....	E5/E3	E5	11.16	52″	0.40	1716	34	−21.5
NGC 1052.....	E4/E2	E3/S0	11.28	37	0.28	1392	28	−20.9
NGC 4697.....	E6/E4	E6	10.03	95	0.36	1210	24	−21.8

NOTES.—Col. (2) and (3) give the galaxy classification from the RC2 and the RSA. Col. (4) gives the total apparent magnitude B_T. Col. (5) lists the effective radius r_e in arcseconds, while col. (6) gives the mean ellipticity from Peletier *et al.* 1990. Col. (7) gives the group velocity in km s^{-1}, and the distance derived from that velocity is given in col. (8), with $H_0 = 50$ km s^{-1} Mpc^{-1}. The absolute magnitude M_B is calculated from B_T and the distance D. The value listed in col. (5) and (7) are taken from Burstein *et al.* 1987 and Davies *et al.* 1987.

major and minor axes of the galaxies and at five intermediate angles spaced at 15° intervals. These galaxies have very small, if any, isophote twists; the largest is a twist in NGC 1052 of only $\approx 7°$ over more than a decade change in radius. For NGC 720 and NGC 4697 the twist is less than 2°–3° over a comparable radius range. The major axes from the CCD images were taken to be 142°, 117°, and 66° for NGC 720, NGC 1052, and NGC 4697, respectively. The entire image of the galaxy was used, each profile being formed by azimuthally averaging the light within a cone of half-angle 7°.5. We assumed that the galaxy images had fourfold symmetry. Both sides of each cut were averaged. For each position angle (other than the major and minor axes), we then averaged the profiles corresponding to equal but opposite angles from the major axis. Thus, we generated seven profiles representing the two-dimensional distribution of light for each galaxy.

The next step was to interpolate each profile onto a grid of 60 points uniformly spaced in log radius. The log surface brightnesses μ at the grid points were obtained from the mean profile of the ray through that point by a combination of (*a*) linear interpolation of μ against log r between adjacent points, and (*b*) least-squares fitting $r^{1/4}$ profiles to sets of three or more nearby points. Near the center, where the grid is denser than the observations, we used simple interpolation. Further out, where there are more than two observations in the radius range covered by a single grid point, we obtained the surface brightness from $r^{1/4}$ profiles fitted to those observations. The surface brightness profiles were extrapolated to values below 20% of the sky brightness by fitting an $r^{1/4}$ profile to each ray over the radius range corresponding to surface brightnesses of twice sky to 20% of sky.

Throughout the above procedure we used the sky-subtracted galaxy images. The papers cited above indicate that the contribution from the night sky can be determined to a precision of only 1%–2%, and they emphasize that this limits the accuracy of the luminosity profiles at large radii.

The CCD data come from two telescope/instrument combinations. The Fairchild 211 CCD was used at the prime focus of the Mayall 4 m telescope on Kitt Peak as described by Jedrzejewski, Davies, and Illingworth (1987), while an RCA CCD was used at the No. 1 0.9 m telescope on Kitt Peak (see Davis *et al.* 1985; Peletier *et al.* 1990). The 4 m data were taken in better seeing than the 0.9 m data and have higher spatial resolution, but smaller radial coverage. At the 4 m telescope the CCD had a pixel size of 0".35 and a field of $\approx 1'.4 \times 1'.6$, compared to 0".86 pixels and a field of $\approx 7' \times 5'$ for the CCD at the 0.9 m telescope. The data from the two telescopes are in excellent agreement, as is shown in Figure 8 of Jedrzejewski, Davies, and Illingworth (1987). The seven radial profiles were generated as described above from each of the these two data sets.

The sky-subtracted 4 m and 0.9 m radial profiles, μ_4 and $\mu_{0.9}$, were combined as follows. The 4 m data were shifted such that the mean of μ_4 over the middle one-third of the data points of the logarithmically spaced radial grid were equal to the mean of $\mu_{0.9}$ in that interval. The log intensity μ in the nth of the $N = 60$ logarithmic radial bins was taken to be:

$$\mu(n) = \begin{cases} \dfrac{3}{2N}\left[n\mu_{0.9} + \left(\dfrac{2}{3}N - n\right)\mu_4\right], & n \le \dfrac{2}{3}N\ ; \\ \mu_{0.9}\ , & n > \dfrac{2}{3}N\ . \end{cases} \quad (1)$$

This scheme gives 100% of the weight to the high-resolution 4 m data in the center, with an increasing contribution of the 0.9 m data until the fortieth bin, beyond which the 0.9 m data contribute 100% to μ. The final radial cuts are shown, offset vertically, in Figure 1.

The absolute calibrations on the Johnson system described in Davis *et al.* (1985) were used. This calibration enters only into the calculation of the total mass-to-light ratio for the fitted model; it does not bear on the issue of whether one can generate reasonable constant mass-to-light ratio models of these galaxies which are consistent with both the luminosity profiles and the measured kinematics.

b) Spectra

The majority of the spectroscopic data used in this work was recorded on baked IIIa-J photographic image-tube plates obtained on the KPNO and CTIO 4 m telescopes using the RC spectrographs. In the case of NGC 1052 these data were supplemented by spectra taken with the KPNO Cryogenic Camera. These latter spectra were obtained, reduced, and analyzed as described in Davies and Illingworth (1986). A complete record of the spectra used here is given in Table 2, together with the exposure times, spectral regions, and slit widths used. The spectral regions used, those around 4200 and 5200 Å, are typical of those generally used for kinematical studies of early-type galaxies.

The kinematic map of NGC 720 consists of three rays passing through the galaxy center—along the major and minor axes and along a ray 30° from the major axis. The maps of NGC 1052 and 4697 are more comprehensive. In addition to the major and minor axis spectra and spectra skewed from these axes, spectra were taken in both galaxies offset from, but parallel to, the major and minor axes. These spectra do not pass through the centers of the galaxies. The slit placement used here is similar to that used by Kormendy and Illingworth (1983) in their kinematic study of the bulges of disk systems. For NGC 1052, spectra were taken along both rays that are 45° from the major axis, as well as parallel to the major axis but offset by 13" to the SW, and perpendicular to the major axis and offset from the minor axis by 15" to the SE. For NGC 4697, spectra were taken along one ray 45° from the major axis, as well as offset by 22" from the minor axis and parallel to it, one to the NE and one to the SW, plus two spectra offset from the major axis and parallel to it, one 10" to the NW and one 20" to the SE. These locations of the slits used for the kinematic maps are shown schematically in Figure 2.

A plate of the full-slit spectrum of the HeNeAr calibration lamp in the spectrograph was recorded with each photographic spectrum to map the geometric distortions. Similarly for each galaxy plate a calibration exposure of comparable exposure time was recorded with the spot sensitometer for use in transforming density to intensity. For each slit width used, spectra of a selection of late G- and early K-type giants stars were taken for use as the velocity and velocity dispersion reference sources. The stars were trailed along the slit to increase the S/N.

The reduction procedures were carried out using the IPPS image processing system at Kitt Peak National Observatory and are described in Illingworth and Schechter (1982) and Davies and Illingworth (1983). The plates of star and galaxy spectra, sensitometer spots, and the HeNeAr lamp were scanned on the PDS microdensitometer at KPNO, and the rasters were transferred to the IPPS where a density-to-intensity transformation was determined and applied. The full-slit

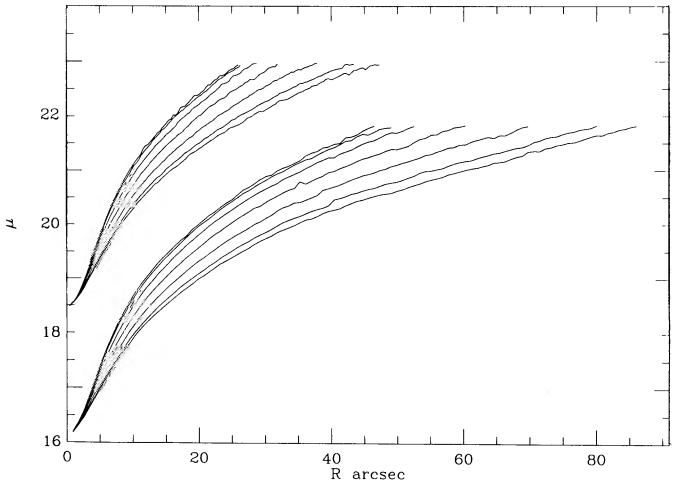

FIG. 1*a*

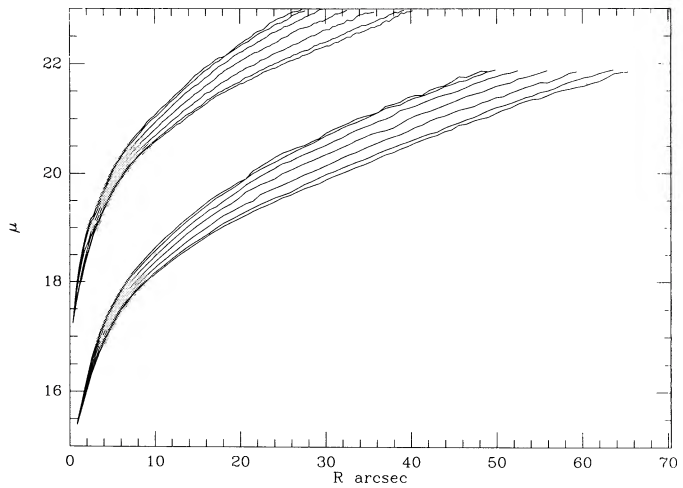

FIG. 1*b*

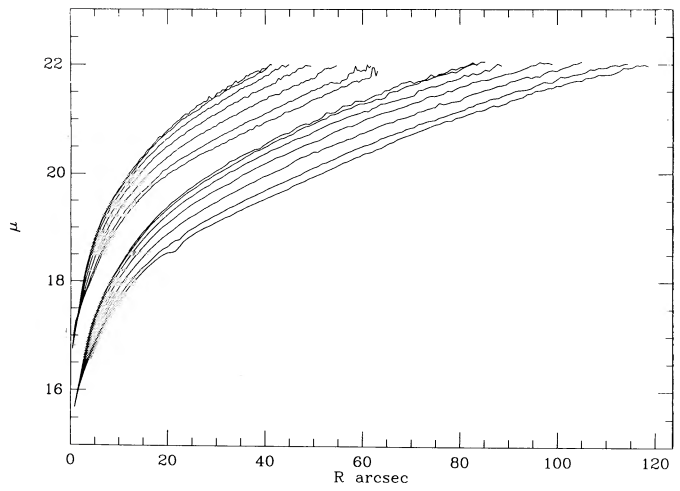

FIG. 1*c*

FIG. 1.—Folded cuts for NGC 720 (*top*), NGC 1052, and NGC 4697 (*bottom*). In each frame the 4 m data have been displaced upwards. Major (*lowest*) and minor (*highest*) axis cuts employ data from two 15° wedges, while the other cuts employ four such wedges.

spectra were then traced, together with the HeNeAr spectra recorded through a decker at the top and bottom of each galaxy/star spectrum. Together these map the distortions and register the distortion map onto the galaxy/star spectra. By fitting Legendre polynomials to the HeNeAr lines and interpolating, the spectra were rewritten onto a logarithmic wavelength scale. Finally, the S-distortion was determined by tracing the center of the spectrum on each plate, fitting and interpolating in a similar fashion.

The instrumental response function along the slit was derived from the variation along the slit in the flux in a strong night-sky emission line. The night sky plus galaxy continuum contaminating the line was determined at each radius by interpolation across neighboring strips of the continuum and was subtracted to give a true line flux. A correction frame was derived by fitting a polynomial to the variation in intensity of the sky line. The resulting instrumental response function was divided into each frame, thereby improving the precision of the sky subtraction. Each frame was cleaned of plate defects, ion events, etc., by interpolation along rows. Regions of the spectrum close to each end of the slit were then averaged together

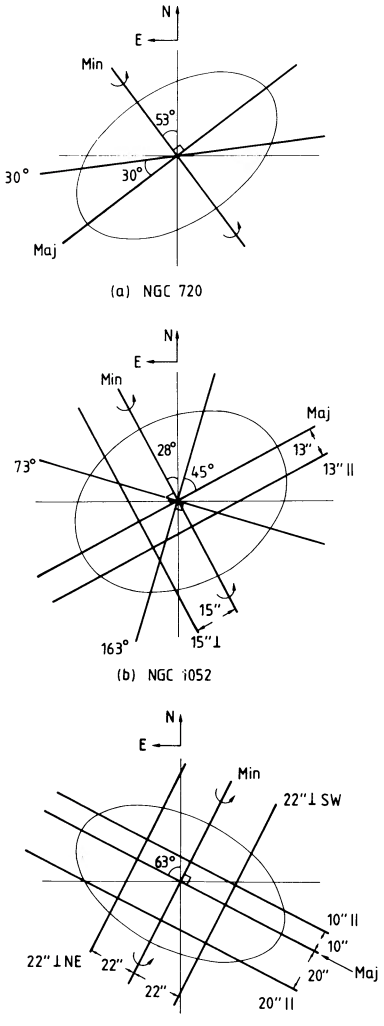

FIG. 2.—Schematic representations of the slit positions used to map the kinematics of NGC 720, 1052, and 4697, and the nomenclature used to describe the different slit positions. Scales for each galaxy for our assumed distances are 0.17, 0.14, and 0.12 kpc arcsec^{-1}, respectively.

TABLE 2

SPECTROSCOPIC OBSERVATIONS

Observatory	Position angle (°)	Slit width (arcsec)	Integration (minutes)	Spectral region (Å)	Comments
(1)	(2)	(3)	(4)	(5)	(6)
		NGC 720 E4 Major Axis (PA 143°)			
CTIO	142	1.1	153	5200 Pg	Major axis (FI)
CTIO	143	2.3	90	4200 Pg	Major axis
CTIO	53	2.3	105	4200 Pg	Minor axis
CTIO	53	2.3	15	4200 Pg	Minor axis
CTIO	113	2.3	134	4200 Pg	Along ray 30°
CTIO	113	2.3	30	4200 Pg	from major axis
		NGC 1052 E4 Major Axis (PA 115°)			
KPNO	118	2.0	90	4200 Pg	Major axis (FI)
KPNO	118	1.6	100	5200 Pg	Major axis (FI)
KPNO	117	2.5	60	5200 Cryo	Major axis
CTIO	115	2.3	18	4200 Pg	Major axis
KPNO	118	1.1	40	5200 Pg	Major axis
CTIO	29	2.3	15	4200 Pg	Minor axis
KPNO	28	2.5	60	5200 Cryo	Minor axis
CTIO	115	2.3	120	4200 Pg	Offset parallel to major axis (13″ SW ∥)
CTIO	29	2.3	135	4200 Pg	Offset parallel to minor axis (15″ SE ⊥)
KPNO	73	1.1	35	4200 Pg	Along 45° ray
KPNO	73	2.5	60	5200 Cryo	Along 45° ray
KPNO	164	2.5	60	5200 Cryo	Along 45° ray
		NGC 4697 E4 Major Axis (PA 63°)			
CTIO	62	1.1	150	5200 Pg	Major axis (FI)
CTIO	64	1.1	150	5200 Pg	Major axis
CTIO	63	2.6	117	4200 Pg	Major axis
CTIO	152	1.1	105	5200 Pg	Minor axis
CTIO	153	2.6	113	4200 Pg	Minor axis
CTIO	153	2.6	120	5200 Pg	Minor axis
CTIO	153	2.6	130	5200 Pg	Offset parallel (22″ NE ⊥)
CTIO	153	2.6	120	5200 Pg	to minor axis (22″ SW ⊥)
CTIO	64	1.1	180	5200 Pg	Offset parallel (10″ NW ∥)
KPNO	64	2.6	67	5200 Pg	to major axis (20″ SE ∥)

NOTES.—The 4 m photographic data were taken with the RC spectrograph and an RCA C33063 image tube plus treated IIIa-J plates, at both CTIO and KPNO. The spectral ranges were typically 3900–4500 Å and 4800–5600 Å for the 4200 and 5200 Å regions, respectively. The instrument dispersion σ_i was typically 120 km s^{-1} in the 5200 Å region and 150 km s^{-1} in the 4200 Å region for the 2″–2.″5 slits. For the 1″ slits, σ_i was typically 80 km s^{-1}.

to generate a sky spectrum which was subtracted from the frame.

Rotation velocities and velocity dispersions were then determined from the rectified and calibrated spectra using the Fourier quotient method that has been widely described and tested, e.g., by Illingworth and Schechter (1982). The full spectral range of the data was used for determining the velocities. However, for the determination of the velocity dispersions the region containing the H and K lines of Ca II was excluded. These features have been shown to bias the results toward higher values (Illingworth and Schechter 1982). Thus the spectra centered at 4200 Å were analyzed twice, once including the H and K features to produce the rotation velocities and once with them excluded to generate the dispersion profiles. The results are presented in Appendix B (Tables 3–5) and in Figures 3–5. As a check on the internal consistency of the results, we have marked on the results from each slit position the velocities and velocity dispersions from the other spectra at the points of intersection. These "overlap" values are shown as open circles on the figures and are the values obtained from a smooth fit to the data of the intersecting spectrum.

In NGC 720 the dispersion profiles along the three rays are in very good agreement; the central value of 260 km s^{-1} also agrees well with the value of 258 km s^{-1} from Davies *et al.* (1987) and 267 km s^{-1} from Schechter (1980). The dispersion falls out to a radius of 10″ beyond which it remains approximately constant at 200 km s^{-1}. There is no evidence of a steeper fall off of the dispersion along the minor axis. The rotation velocity on the 30° ray is constant and very close in amplitude to that on the major axis out to a radius of 30″. At larger radii the rotation curve on the major axis rises to 100 km s^{-1}. The rotational velocity on the minor axis is consistent with zero.

In NGC 1052 the velocity dispersion rises to a peak of 240 km s^{-1} in the center from 190 km s^{-1} at 10″ radius. This behavior is seen on all rays. Beyond 10″ the dispersion is consistent with being constant (out to the limit of the data at 45″). The major-axis rotation curve reaches 80 km s^{-1} at 5″–10″ and then increases more slowly to 100 km s^{-1}, changing very little from 15″ to 45″. A small but significant rotation velocity on the minor axis (15 km s^{-1}) is detected (see Davies and Illingworth 1986 for a discussion of this). The parallel cut at 13″ shows that the rotation velocity asymptotes to 80 km s^{-1}. The slow fall of velocity away from the major axis is confirmed by the 15″ perpendicular cut.

The major-axis rotation curve of NGC 4697 reaches a

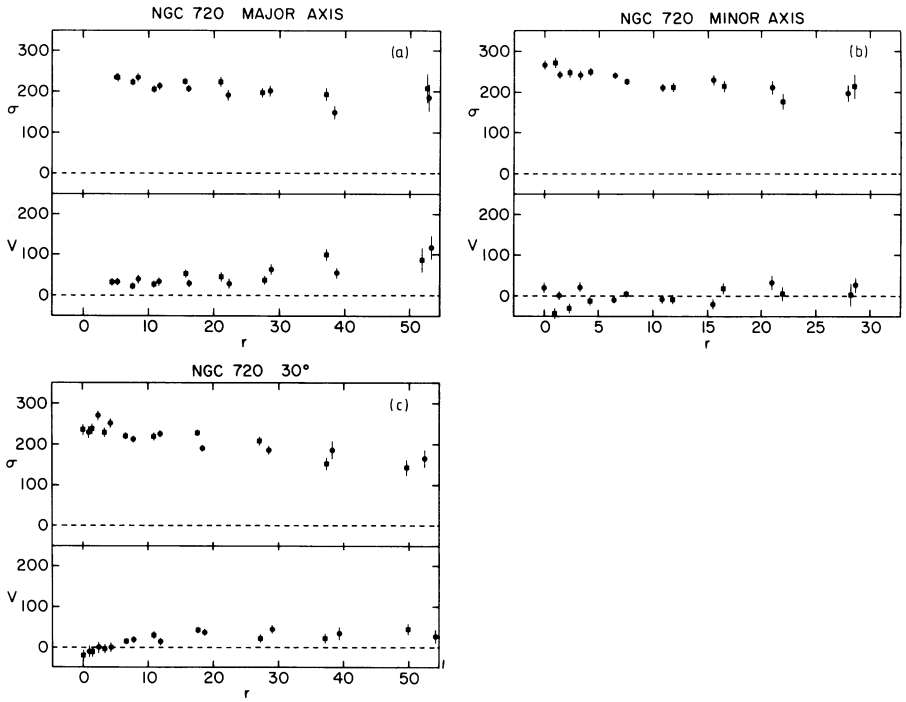

FIG. 3.—Velocity dispersion (σ) and rotation velocity (v) as a function of radius for NGC 720 along the major and minor axes and at position angle 30° from the major axis. Filled circles are radii to the east of north along the major and minor axes, but to the west of north along the 30° ray. The galaxy is rotating such that points to the NW of the nucleus are receding.

maximum of 100 km s^{-1} at 4″ and remains essentially constant out to a radius beyond 60″. The perpendicular and parallel cuts are strikingly consistent and show that the rotation velocity falls off more rapidly away from the major axis than in NGC 1052 (which is comparable in distance and size). The velocity dispersion is remarkably constant, decreasing by less than 10% from its central value of 180 km s^{-1} out to a radius of 1′.

III. THE MODELS

Although it is now generally accepted that most elliptical galaxies are probably triaxial, it nonetheless is interesting to compare our data with the simplest dynamical models, namely axisymmetric systems in which the velocity dispersion tensor is everywhere isotropic. Such comparisons are helpful because (i) the structure of a mildly triaxial system is likely to resemble closely that of an axisymmetric system, and (ii) by studying differences between simple axisymmetric models and real galaxies we are likely to gain valuable guidance as to what kinds of triaxial systems will ultimately provide satisfactory models of observed systems. We have tailored axisymmetric models to each galaxy by the following three-step process:

1. The luminosity profiles are inverted to get the three-dimensional luminosity density, and hence the mass density with our assumption of constant mass-to-light ratio;

2. The potential is evaluated, and the velocity dispersion and azimuthal streaming are derived assuming that the distribution function is of the form $f(E, L_z)$ and, initially, that the velocity dispersion is isotropic;

3. The projected kinematical quantities from the model are compared with the velocity and velocity dispersion profiles, and iterated, if necessary, by adding the contribution from a disk or by dropping the isotropy constraint and changing the ratio of azimuthal to radial dispersion.

a) Derivation of a Three-dimensional Luminosity Model

The first step is to least-squares fit either a flattened Jaffe (1983) model or a flattened modified Hubble model (Rood *et al.* 1972) to the surface brightnesses at the grid points. A Jaffe model is useful at this stage because it provides a simple approximation to the three-dimensional density of the $r^{1/4}$ model and can be analytically projected down any line of sight. The three-dimensional density of a Jaffe model diverges at small r as r^{-2}. Although such singular central behavior is appropriate for some galaxies such as NGC 1052, it is a poorer fit to others such as NGC 720. The finite central density of the modified Hubble model is a good fit to NGC 720.

We have not explicitly corrected for the effects of seeing but can gauge the importance of seeing for the final velocity profiles by comparing results obtained from an initial fit to a Jaffe model with those obtained by initially fitting with a modified Hubble model; in models of the first type the central surface brightness is always brighter than in models of the second type, even though the difference decreases with the number of Lucy iterations performed (see below). After carrying out a few Lucy iterations such that the difference in surface brightness between these two models is comparable to that expected from seeing (see PDIDC), we find that the difference of the predicted kinematics is only very small (van der Marel, Binney, and Davies 1990).

The initial least-squares fit of a three-parameter spheroid to the seven surface brightness profiles is then relaxed onto the observations by means of Lucy's (1974) iterative algorithm. We derive the necessary formulae in Appendix A. Let R be the radius in the galaxy's symmetry plane and z denote distance down to the line of sight. Then the relaxation proceeds as follows: (i) the surface brightness I_n at each grid point on the

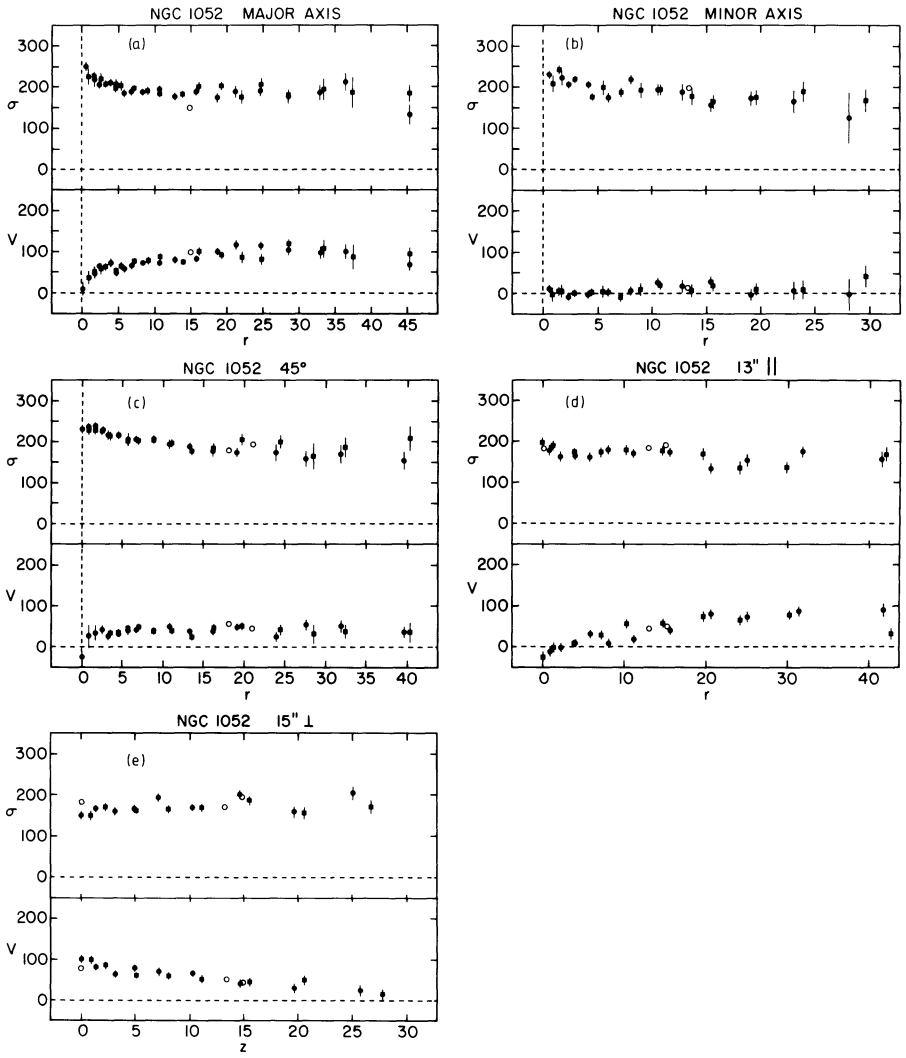

FIG. 4.—As Fig. 3, but for NGC 1052 along the major axis and the minor axis, along a ray 45° from the principal axes, along a slit offset parallel to the major axis by 13″, and along a slit offset perpendicular to the major axis 15″ from the minor axis. Filled circles correspond to points to the west of north. The galaxy is rotating such that points to the NW are receding. Note that along the slit offset from the minor axis by 15″ the velocities have been plotted as positive, although they are actually all negative since the slit is to the SE of the nucleus. Along this slit, filled circles represent measurements made to the NE of the major axis. Open circles indicate measurements made at another slit position where that slit intersects the panel's slit; see the intersection points of the slits in Fig. 2 for a visual guide to their locations and radii.

sky is estimated by numerically integrating the current estimate of the luminosity density $j_n(R, z)$ along the appropriate line of sight, (ii) from these brightness estimates and the observed surface brightnesses I_{obs} we form the ratios $f_n \equiv I_{obs}/I_n$; (iii) new density estimates $j_{n+1}(R, z)$ are now obtained by multiplying each $j_n(R, z)$ by the integral of f times a certain kernel around the ellipse on the sky onto which the hoop of brightness (R = const, z = const) projects; (iv) the ratios f_{n+1} to which these revised densities give rise are calculated, and, if they are considered unsatisfactory, new densities j_{n+2} are calculated.

The case of NGC 1052 will illustrate the effectiveness of this scheme. For an assumed inclination $i = 80°$, the least-squares fit of a Jaffe model yields an rms residual of 0.27 mag. After successive Lucy iterations the residuals become 0.089, 0.048, 0.033, and 0.026 mag. At each iteration some of the power at high spatial frequencies generated in the data by dust and/or imperfectly removed stars seeps into the model's three-dimensional density distribution. Once the three-dimensional density profile has become jagged, it cannot be the profile of a hot stellar system and will yield physical nonsense when one solves the Jeans equations for the associated dynamical variables. Consequently, one must be content with residuals of a few hundredths of a magnitude, even though such residuals may be larger than the internal errors of the photometry. This is not a significant problem, however, since comparison of our photometry with other reliable photometry of the same galaxies indicates that the external errors are probably as large as the residuals of our models.

Since some oblate galaxies may contain disks that are approximately exponential, we have experimented with including an exponential disk in the fit. Initial fits obtained by simultaneously varying the three free parameters of the spheroid and the two free parameters of the exponential disk do not yield realistic models—implausibly luminous disks are fitted. It is clear that the spheroid model is not a highly accurate representation of the spheroid data, and so the fitting routine uses the disk parameters primarily to improve the radial fit, resulting in

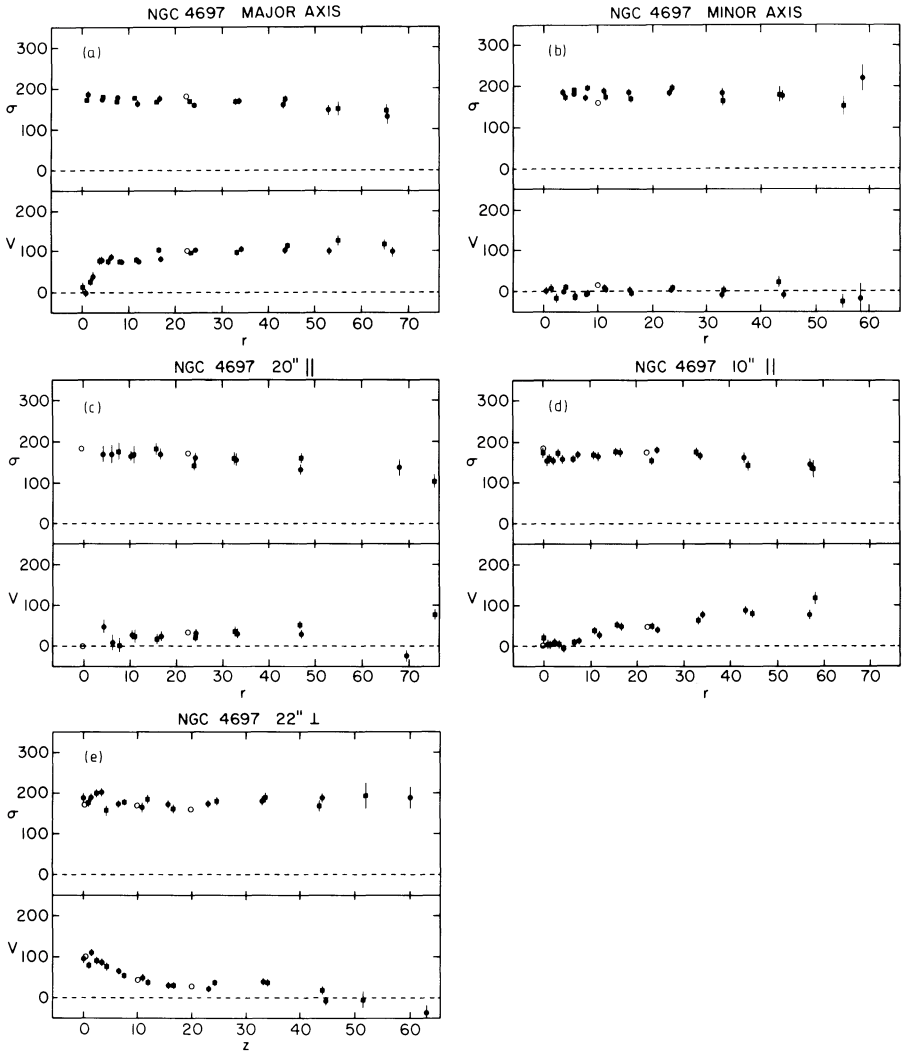

FIG. 5.—As Fig. 3, but for NGC 4697 along the major axis and the minor axis, along slits offset parallel to the major axis by 10″ to the NW and 20″ to the SE, and along slits offset perpendicular to the major axis 22″ from the minor axis both to the NE and the SW (these have been averaged together to produce a single panel of higher S/N data). Filled circles generally indicate points to the west of north. However, on the minor axis this convention is reversed, filled circles representing points to the east of north, and for the spectra offset by 22″ from the minor axis the filled circles represent points to the SE of the major axis. The galaxy is rotating such that points to the SW of the nucleus are receding. Again, as in Fig. 4, open circles indicate measurements made at another slit position where that slit intersects the panel's slit; see Fig. 2 for the intersection points.

"disks" that dominate the surface brightness at some radii. Increasing the number of rays beyond seven and constraining, in some way, the disk model to fitting the azimuthal deviations might improve the effectiveness with which disk models are fitted. However, in view of these problems, we decided to select the disk parameters *a priori* when the results of others suggested that a disk should be included. We then substracted the disk brightness distribution from the observations and fitted the residual light with a spheroid as described above. The contributions to the potential of both the disk and the spheroid were then derived independently as described below.

b) *Evaluation of the Dynamical Quantities*

We assume that the spheroid's mass density $\rho(R, z) = \Upsilon_s j(R, z)$, where Υ_s is some constant mass-to-light ratio, and obtain the gravitational potential Φ_s generated by the spheroid in the form

$$\Phi_s(R, z) = \sum_{l=0}^{5} \tilde{\Phi}_l(R) P_{2l}\left(\frac{z}{\sqrt{R^2 + z^2}}\right), \qquad (2)$$

where P_k is the Legendre polynomial of order k. The quantities $\tilde{\Phi}_l(R)$ are obtained by (i) six-point Gaussian evaluation of the integrals

$$\tilde{\rho}_l(r) = \int_0^1 \rho(r\sin\theta, r\cos\theta) P_{2l}(\cos\theta)\, d(\cos\theta) \qquad (3)$$

on a logarithmic grid of r values, (ii) direct evaluation of the integrals

$$\tilde{\Phi}_l(r) = -4\pi G\left[\frac{1}{r^{2l+1}}\int_0^r \rho_l(s) s^{2l+2}\, ds + r^{2l}\int_r^\infty \rho_l(s)\frac{ds}{s^{2l-1}}\right] \qquad (4)$$

for these r values, and (iii) linear interpolation of $\tilde{\Phi}_l$ versus $\log r$.

The disk, if included, is assumed to have mass-to-light ratio Υ_d. By Toomre (1962) and Freeman (1970), the disk potential is

$$\Phi_d = -\frac{2\pi G \Upsilon_d I_d(0)}{R_d}\int_0^\infty \frac{J_0(kR)e^{-kz}}{(R_d^{-2} + k^2)^{3/2}}\, dk\,. \qquad (5)$$

For $z = 0$ this integral can be evaluated analytically. For

$z \neq 0$, $R \neq 0$ the integral must be evaluated numerically. For $R = 0$ we have

$$\Phi_d(0, z) = -2\pi G \Upsilon_d I_d(0) z \left\{ \frac{\pi}{2} \left[H_1\left(\frac{z}{R_d}\right) - Y_1\left(\frac{z}{R_d}\right) \right] - 1 \right\}, \tag{6a}$$

where Y_1 is the usual Bessel function and the Struve function H_1 may be evaluated as

$$H_1(x) = \frac{2x^2}{\pi} \left[3\left(\frac{1}{3!!}\right)^2 - 5\left(\frac{x}{5!!}\right)^2 + 7\left(\frac{x^2}{7!!}\right)^2 + \cdots \right]. \tag{6b}$$

Once the potential $\Phi = \Phi_s + \Phi_d$ and the luminosity density j are known, the velocity dispersion σ in the meridional directions expected if the system has a distribution function of the form $f(E, L_z)$ is given by (Satoh 1980)

$$\sigma^2(R, z) = \frac{1}{j(R, z)} \int_z^\infty j \, d\Phi , \tag{7}$$

where the integral is along a line of constant R. The mean-square azimuthal speed $\overline{v_\phi^2}$ now follows as (Satoh 1980)

$$\overline{v_\phi^2} = \sigma^2 + R \frac{\partial \Phi}{\partial R} + \frac{R}{j} \frac{\partial (j\sigma^2)}{\partial R} . \tag{8}$$

The density distribution determines only the part of $f(E, L_z)$ that is even in L_z (Lynden-Bell 1962; Dejonghe 1986). Therefore, without further assumptions one cannot separate $\overline{v_\phi^2}$ into the contribution σ_ϕ^2 from the azimuthal velocity dispersion and the contribution $\bar{v}_\phi^2$ from the mean stellar motion. A natural assumption is that (Satoh 1980)

$$\bar{v}_\phi = k\sqrt{\overline{v_\phi^2} - \sigma^2} = k\sqrt{R \frac{\partial \Phi}{\partial R} + \frac{R}{j} \frac{\partial (j\sigma^2)}{\partial R}} , \tag{9}$$

where k is some constant such that $k = 1$ for isotropic velocity dispersion. Then

$$\sigma_\phi^2 \equiv \overline{v_\phi^2} - \bar{v}_\phi^2 = k^2\sigma^2 + (1 - k^2)\overline{v_\phi^2} . \tag{10a}$$

Another way of expressing this relation is

$$\sigma_\phi^2 - \sigma^2 = (1 - k^2)(\overline{v_\phi^2} - \sigma^2) . \tag{10b}$$

In all models $(\overline{v_\phi^2} - \sigma^2) > 0$, so when $k < 1$ the azimuthal velocity dispersion exceeds the radial dispersion σ rather than being smaller than σ, as is the case in the solar neighborhood.

We have tested our programs by having them recover some of Satoh's (1980) analytical results. The recovered velocity dispersions are accurate to better than 1%, except near the grid's outer edge where the error can be as large as 5%. The recovered streaming velocities are significantly less accurate, with a typical error of a few percent. At the center and close to the minor axis, where the rotation velocity makes only a small contribution to the system's dynamics and is therefore recovered as the small difference of large numbers, the streaming velocities can be in error by more than 10%, even away from the edges of the grid. Errors of this order seem to be inescapable given the number of points on the grids from which we infer dynamical quantities (van der Marel, Binney, and Davis 1990). In any event, the fractional observational errors in the streaming velocities are also large near the minor axis, so the theoretical uncertainties of our models are nonetheless everywhere smaller than the observational errors. van der Marel, Binney, and Davies demonstrate the insensitivity of our implementation of Lucy's algorithm to noise in the data.

IV. CONFRONTATION OF MODELS WITH OBSERVATIONS

Three parameters are available to us when fitting observations of a particular galaxy: (i) the mass-to-light ratio Υ; (ii) the azimuthal versus radial velocity dispersion anisotropy parameter k of equations (8)–(10); and (iii) the inclination i of the galaxy. The minor-axis velocity dispersion profile is strictly independent of k and drops slightly as i is lowered below 90°, so Υ, the R-band mass-to-light ratio, is chosen to optimize the agreement between observation and the predicted minor-axis velocity dispersion profile.

Decreasing the inclination causes the model to become intrinsically flatter and, therefore, more strongly affected by rotation (at fixed k). Hence, at fixed Υ decreasing i lowers the predicted minor-axis dispersion profile. If k is also held constant as i is lowered, the model's major-axis dispersions drop while the major-axis rotation velocities rise.

With $k = 1$ and $i = 90°$ the model will lie close to the oblate line in the $(\epsilon, v/\sigma)$-plane. Decreasing k lowers the model in this plane, while decreasing i raises the model.

a) NGC 720

The right panel of Figure 6 shows $\mu_{\rm model} - \mu_{\rm obs}$ after 1–4 Lucy iterations from a modified Hubble fit; the full curve corresponds to the final model. Sets of curves are shown for only four rays, the major axis being at top and the minor axis at bottom. A perfect model of perfect data would follow the dotted lines. The rms difference is 0.058 mag. The left panel shows the density distribution of the final model along each selected ray for an assumed distance of 34 Mpc.

Figure 7 shows the fit we obtain to our observations of the kinematics of NGC 720. The full curves are for an assumed inclination $i = 90°$, isotropic velocity dispersion ($k = 1$), and mass-to-light ratio $\Upsilon = 5.8\ \Upsilon_\odot$ (in R-band units). In this, as in every other case, Υ has been chosen by eye fitting to optimize

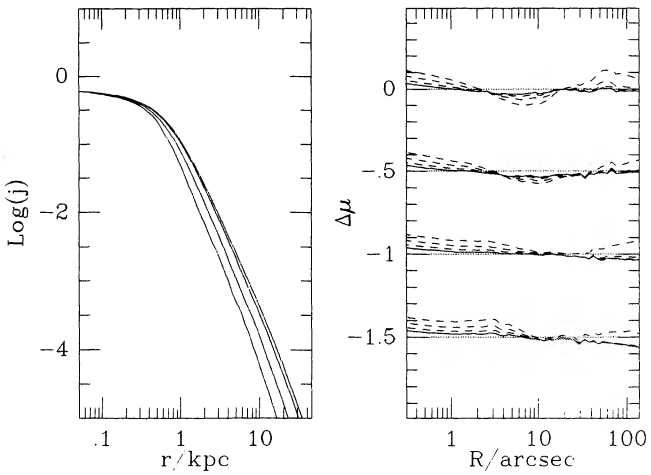

FIG. 6.—The sets of curves at right show the residual surface brightness $\mu_{\rm model} - \mu_{\rm obs}$ after each Lucy iteration from an initial modified Hubble fit to NGC 720. Residuals are shown for just four of the seven rays, with the major axis being the top set and the minor axis the bottom set. Exact agreement corresponds to the curves running along the dotted lines. Where a curve is below its dotted line, the model is brighter than the galaxy. The full curves correspond to the adopted model. The left panel shows the final density profile in units of $10^{10}\ L_\odot\ {\rm kpc}^{-3}$ for each of the rays plotted at the right.

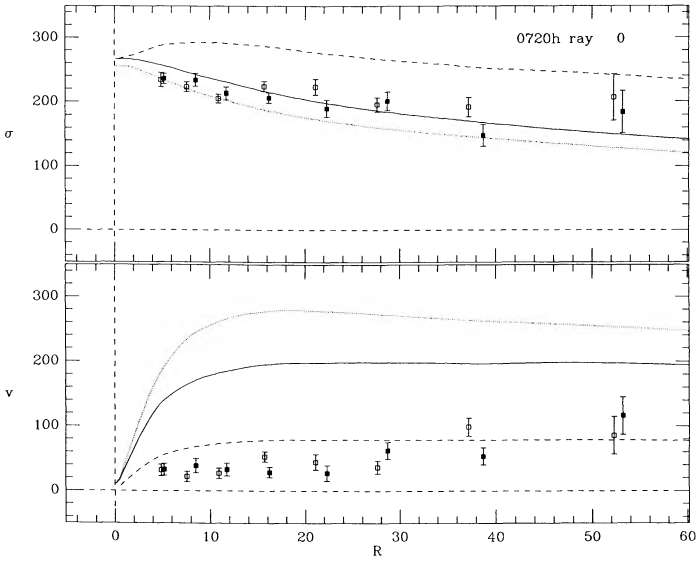

FIG. 7a

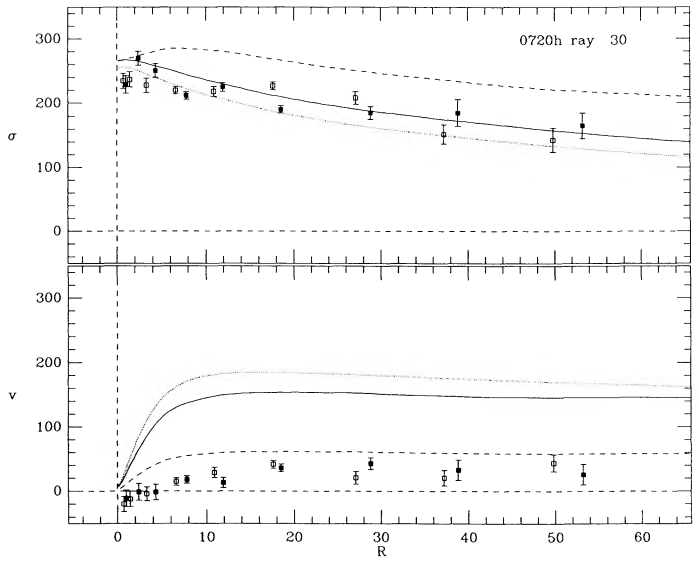

FIG. 7c

FIG. 7.—Predicted and observed kinematics of NGC 720. Legends at top right of each panel indicate the relevant slit position with respect to the major axis. Full curves are obtained with inclination $i = 90°$ and anisotropy parameter $k = 1$. Dotted curves (*thin lines*) are for $k = 1$ and $i = 65°$. Dashed curves are for $i = 90°$ and $k = 0.4$.

agreement between the observed and predicted velocity dispersions along the minor axis. The form of the model dispersion profile matches the data quite well (note that Υ has been chosen to optimize the normalization of this profile). Along the major axis the predicted velocity dispersion falls too steeply, while the predicted rotation velocity is grossly excessive. Along the 30° ray the velocity dispersions are in reasonable agreement, but the predicted rotation speed is again much too high.

The dotted curves in Figure 7 show the effect of assuming an inclination $i = 65°$. At this inclination the galaxy has to be intrinsically significantly flatter ($b/a \simeq 0.332$ compared to 0.519 at $i = 90°$) and therefore (so long as $k = 1$) more nearly supported by rotation than random motion. Thus, when $i = 65°$ the dispersion curves are lower and the rotation curves higher than when $i = 90°$, contrary to one's initial intuitive response.

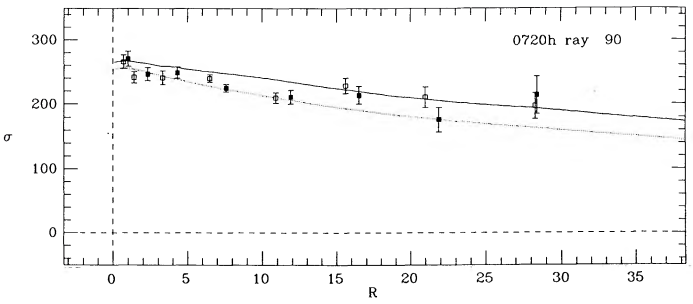

FIG. 7b

The increase needed due to the greater flattening offsets the projection factor.

The dashed curves in Figure 7 show the effect of assuming $i = 90°$ and $\Upsilon = 5.8\ \Upsilon_\odot$ as for the full curves, but dropping k to 0.4. The theoretical dispersion profile is indistinguishable along the minor axis. On the major axis the predicted rotation speed is now of the right order, although the theoretical curve is still too high near the center. However, with $k = 0.4$ the predicted velocity dispersion on the major axis is much too high. The situation is very similar along the 30° ray. Thus we can firmly state that NGC 720 *cannot have a distribution function of the form* $f(E, L_z)$.

b) *NGC 1052*

Figure 8 shows the fit obtained to our photometry of NGC 1052 after three Lucy iterations from a Jaffe model; since this galaxy does not have a resolved core, a Jaffe model leads to a much better fit than a modified Hubble profile. The rms residual is 0.039 mag.

The full curves in Figure 9 show the kinematics predicted by setting $\Upsilon = 4.5\ \Upsilon_\odot$ and $k = 1$ at an assumed distance $D = 28$ Mpc. Theory and observation are in good agreement along the minor axis. As in the case of NGC 720, there is a tendency for the velocity dispersion to fall too steeply on the major axis and the predicted major-axis rotation curve to be too high. The discrepancies are not as large, however, as for NGC 720.

The dashed curves in Figure 9 show the effect of lowering k to 0.7. The predicted major-axis rotation curve is now in good agreement with observation, while the measured major-axis dispersions are still in reasonable agreement with theory. With $k = 0.7$ theory and observation are also in reasonable agree-

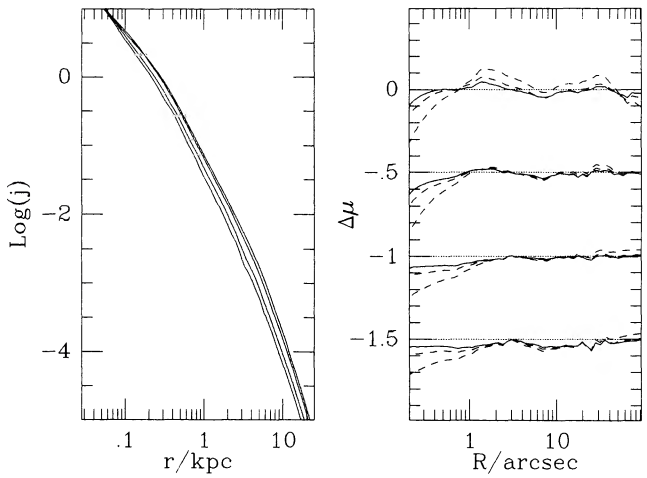

FIG. 8.—Same as Fig. 6, but for NGC 1052

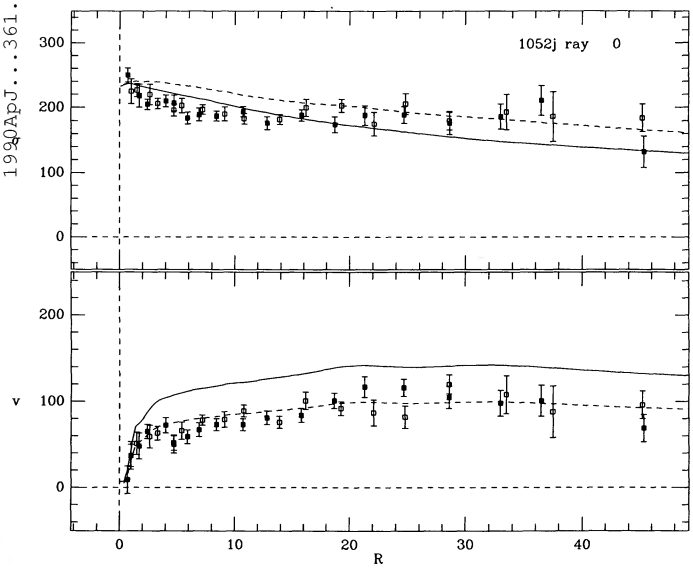

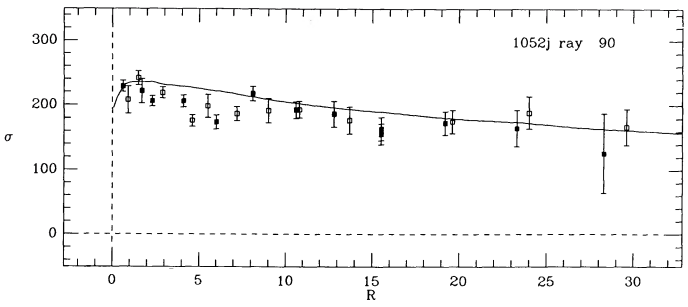

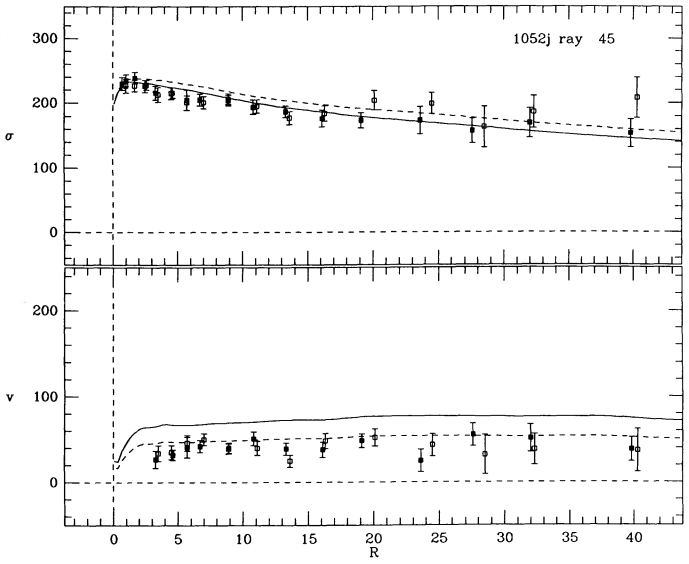

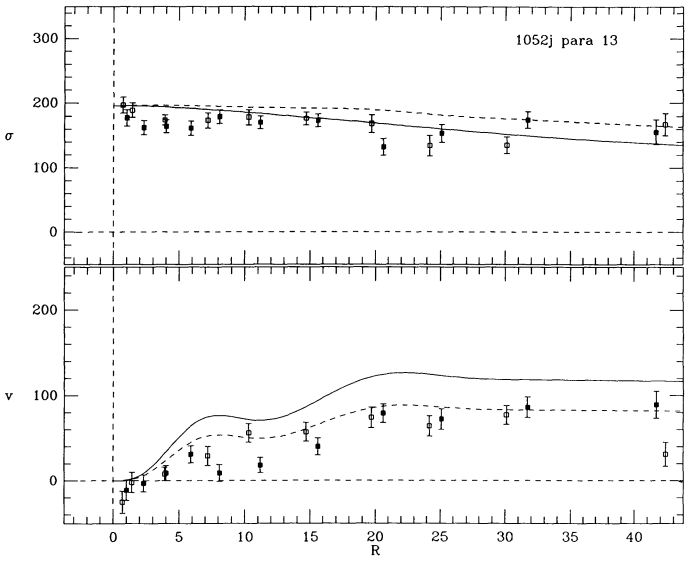

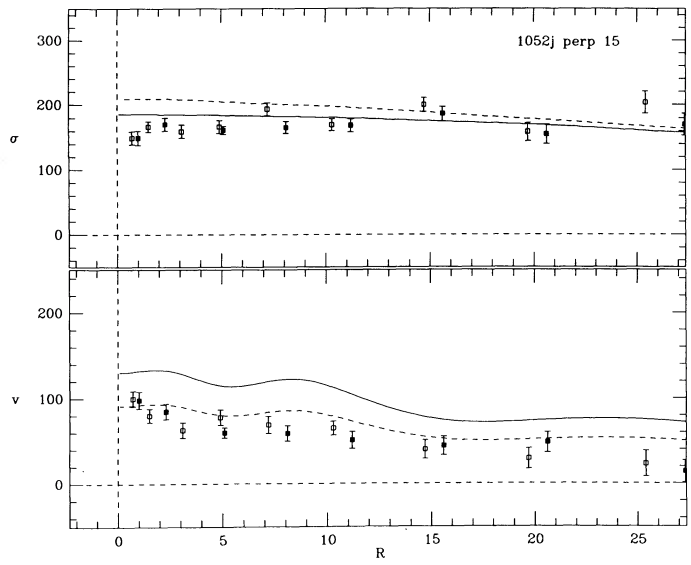

FIG. 9.—Same as Fig. 7, except for NGC 1052. Dashed curves (*thin lines*) now correspond to $i = 90°$, $k = 0.7$.

ment along the 45° ray and the cut parallel to the major axis that passes 13″ from the nucleus. Thus, the gross structure of the kinematics of NGC 1052 are consistent with the galaxy having a distribution function of the form $f(E, L_z)$.

The predicted rotation velocities along the cut 13″ above the major axis show remarkable shoulders between 7″ and 12″ from the symmetry axis. These features are numerical artifacts introduced by our azimuthal interpolation scheme (van der Marel, Binney, and Davies 1990). The wiggles in the cut that runs perpendicular to the major axis are another manisfestation of this phenomenon. These features disappear when cubic splines are used to interpolate in both the radial and azimuthal directions, and the shoulderless profiles then generated are simply smoothed versions of the profiles. Thus, they do affect the results.

c) *NGC 4697*

The core of NGC 4697 is less well resolved than that of NGC 720 but better resolved than that of NGC 1052. Consequently, adequate fits to the photometry of NGC 4697 can be obtained starting from either a Jaffe model or a simplified Hubble profile. However, we show here the results obtained from a Jaffe model, since these encompass a crude correction for the effects of seeing. The corresponding curves for models obtained by iterating on a modified Hubble profile differ by at most 8 km s^{-1}, and usually very much less, the central dispersions being slightly larger and the rotation velocities correspondingly smaller.

Figure 10 shows the final model (for a distance $D = 24$ Mpc) and the residuals after each of three Lucy iterations—the final rms residual is 0.041 mag. Note the final density profile is more jagged, especially along the minor axis, than are our models of NGC 720 and NGC 1052. The sharp kink in the minor-axis profile $r \simeq 0.16$ kpc (1″.7) emerges rapidly on Lucy iteration from either a Jaffe or a modified Hubble starting point and results from the close bunching of the 4 m profiles at $R \simeq 2''$ to be seen in Figure 10.

The full curves in Figure 11 show the kinematics predicted by setting $\Upsilon = 2.8\ \Upsilon_\odot$ and $k = 1$. The fit to the observed dispersions on the major and minor axes and the cut parallel to the major axis and displaced 20″ from it are all excellent. Along our other two cuts the agreement between theory and the observed dispersions is less good but adequate.

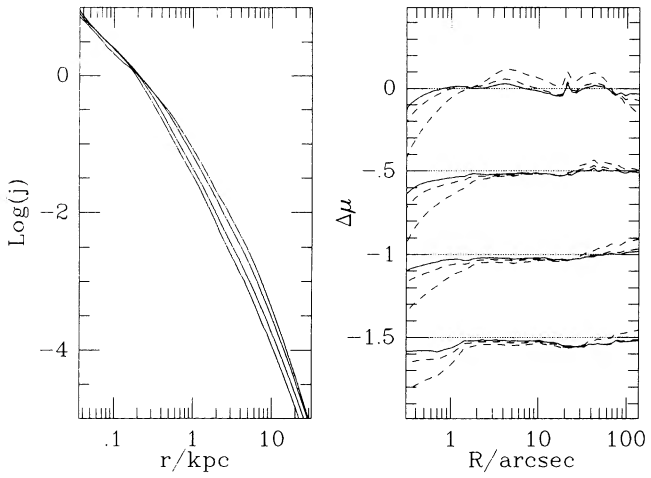

FIG. 10.—Same as Fig. 6, but for NGC 4697

However, the rotation velocities predicted by $k = 1$ are consistently too high, especially along the 20″ parallel cut. The dashed curves in Figure 11 show the result of lowering k to 0.77. Theory and observation are now in good agreement on both major and minor axes. This is less true away from the principal axes: the predicted dispersions are in fair agreement with observation both parallel and perpendicular to the major axis, but the predicted rotation velocities are still significantly too large away from the major axis. As in the case of NGC 1052, our interpolation scheme gives rise to unreal shoulders in the predicted velocities parallel to the major axis between the fourth and fifth rays, and to similar artifacts in the other off-axis velocity cuts.

The central isophotes of NGC 4697 are slightly pointed like those of a nearly edge-on disk (Carter 1987; Jedrzejewski, Davies, and Illingworth 1987). It is interesting to ask how the kinematics of this galaxy would be affected by the presence of a disk? Carter (1987) estimates that a disk in NGC 4697 can nowhere contribute more than 13% of the surface brightness. The dotted curves in Figure 11 show the kinematic profiles obtained by including a thin exponential disk with scale length 3 kpc which contains 4% of the galaxy's total mass and 5% of its luminosity. Since an exactly edge-on disk of dynamically negligible mass would be photometrically obvious, the dotted curves assume an inclination $i = 70°$ for the galaxy. At this inclination the disk contributes up to 20% of the aggregate surface brightness. It will be seen that the only significant difference between the disk model and the diskless model (with $i = 90°$) is that in the disk model the predicted rotation speeds are slightly larger near the center. There is no significant difference between the models in the variation of rotation velocity with distance from the major axis.

Together the comparisons of the models with the data for NGC 4697 suggest that the distribution function is not of the form $f(E, L_z)$. The result is less strong, however, than in the case of NGC 720.

d) *Is the Mass-to-Light Ratio Constant?*

Since the predicted minor-axis velocity dispersion profiles are relatively insensitive to the free parameters of our models, it is interesting to examine these for evidence that the mass-to-light ratio Υ changes with radius. While the predicted dispersion curves of NGC 4697 do not pass through all formal error bars, they clearly lie within the band of uncertainty which is implied by comparison of the measured points on each side of the nucleus. The cases of NGCs 720 and 1052 are slightly more complex in that the predicted profiles pass through the formal error bars at the center and for large R but lie consistently above the data in intermediate ranges of R. NGC 1052 clearly has a compact nucleus, and improper correction for the effects of seeing on both photometry and spectroscopy is likely to account for this discrepancy.

The predicted major-axis velocity dispersion profiles are sensitive, unfortunately, to the free parameters of the results. However, a consistent impression is obtained that the predicted profiles fall more steeply with R than the data warrant. This impression is particularly strong in the case of NGC 1052, which is the galaxy we are otherwise best able to model. This effect may arise from a radial increase in Υ. Alternatively, since a satisfactory profile would follow the full curve ($k = 1$) in Figure 9 for $R \lesssim 20''$ and then transfer to the dashed curve ($k = 0.7$) it is entirely probable that Υ is constant withing the

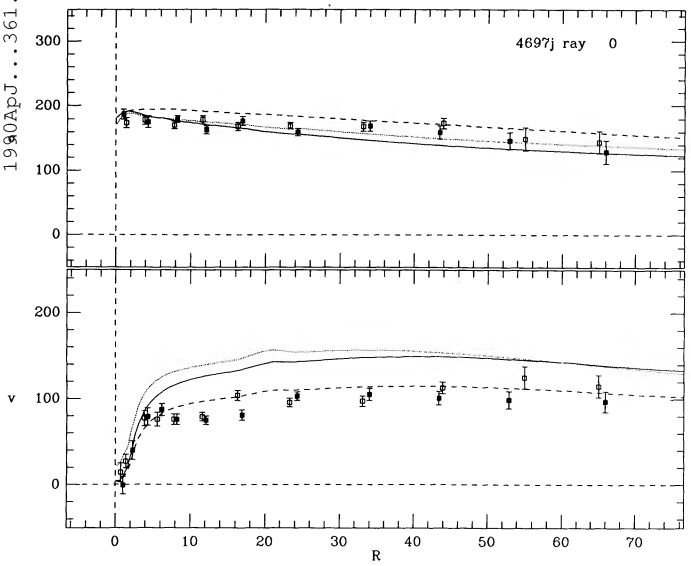

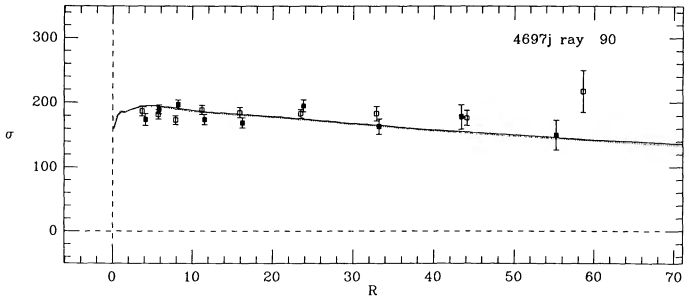

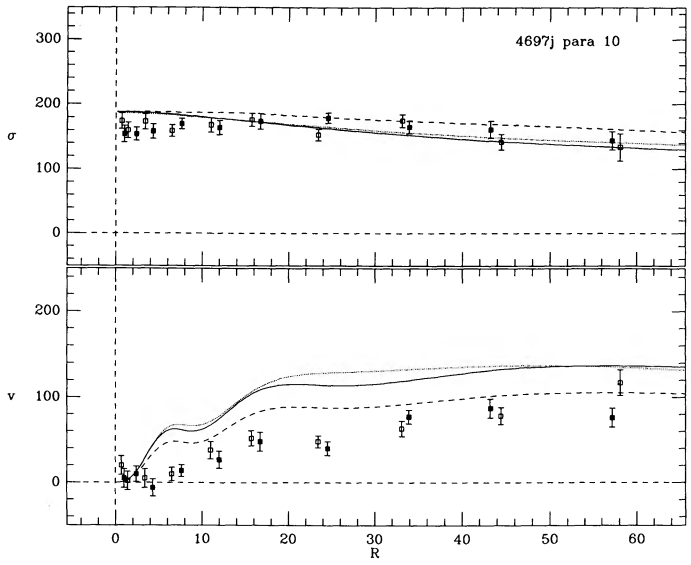

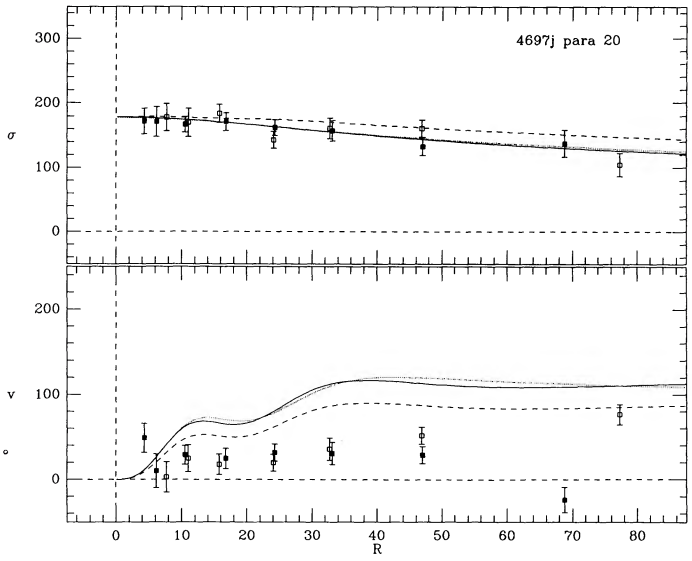

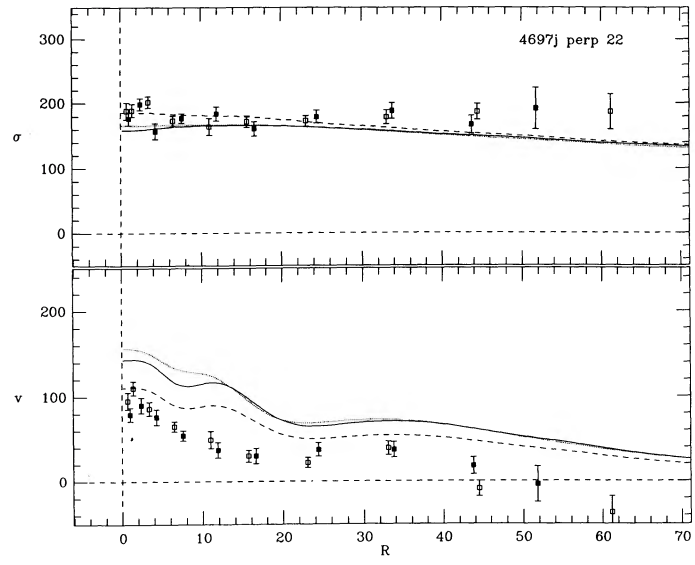

FIG. 11.—Same as Fig. 7, but for NGC 4697. Full and dashed curves correspond to models with inclination $i = 90°$ and $\Upsilon = 2.8\ \Upsilon_{\odot}$. For the full curves $k = 1$, while the dashed curves correspond to $k = 0.77$. Dotted curves are for a model with inclination $i = 70°$ in which 4% of the galaxy's mass and 5% of its light is invested in a thin exponential disk with scale length 3 kpc. In this disk model the bulge mass-to-light ratio is still $\Upsilon = 2.8\ \Upsilon_{\odot}$.

studied range of NGC 1052 and that the distribution function of this galaxy is not of the simple form assumed here.

In R-band units with $M_R(\odot) = 4.31$ (Allen 1973; p. 162; Bessell 1979) the mass-to-light ratios Υ_R are $5.8h_{50}$, $4.5h_{50}$, and $2.8h_{50}$ for NGC 720, NGC 1052, and NGC 4697, respectively. These values are for distances of $34h_{50}^{-1}$ Mpc, $28h_{50}^{-1}$ Mpc, and $24h_{50}^{-1}$ Mpc, respectively. The corresponding mass-to-light ratios in B-band units are Υ_B of $10.3h_{50}$, $8.0h_{50}$, and $5.0h_{50}$, where we have assumed $(B-R)_J(\odot) = 1.17$ (Allen 1973) and $(B-R)_J$(galaxy) = 1.8 (Peletier *et al.* 1989).

Our estimate of Υ for NGC 720 may be significantly high: in § IV*a* we demonstrated that the distribution function of NGC 720 must be of the form $F(E, L_z, I_3)$, whereas our estimate of Υ is obtained by matching the minor-axis dispersion profile to the best fitting model with $F(E, L_z)$. This model will, for given Υ, underestimate the minor-axis dispersions since the model will be flattened by enhanced $\overline{v_\phi^2}$, which does not contribute to the minor-axis profile, while the real galaxy is flattened by enhanced $\overline{v_r^2}$, which does contribute on the minor axis. Hence on fitting such a model to the observed minor-axis dispersions one will tend to *overestimate* Υ. Consequently, for NGC 720 we have $\Upsilon_B < 10.3(34h_{50}/D)$.

V. SUMMARY

We have presented extensive long-slit spectroscopy of the flattened ($\approx$E4) ellipticals NGC 720, 1052, and 4697, with spectra being obtained along directions that are parallel but offset from the major and minor axes, as well as along these principal axes and at skew angles to them.

From CCD photometry of these galaxies we have derived three-dimensional axisymmetric models of the underlying luminosity distributions. The photometry can be equally well fitted for a range of assumed inclinations around $i = 90°$. Our models fit the data to within $\lesssim$0.05 mag. Closer fits to the data could have been obtained by iterating Lucy's cycle a few more times. However, the data contain kinks and blips due to dust and/or imperfectly removed stars, and on each iteration some of the power at high spatial frequencies that is generated by these features seeps into the three-dimensional model. Once the three-dimensional density profile has become jagged, it cannot be the profile of a hot stellar system. Consequently, physical nonsense will be produced when one solves the Jeans equations for the dynamical variables associated with a jagged density profile. Therefore, we have contended ourselves with residuals of a few hundredths of a magnitude, even though such residuals are larger than the internal errors of our photometry. Comparison of our photometry with other reliable photometry of the same galaxies indicates that the external errors are probably as large as 0.04 mag.

We use the Jeans equations to derive line-of-sight velocity dispersion and streaming velocity fields from these three-dimensional models under the assumptions of constant mass-to-light ratio Υ and a distribution function of the form $f(E, L_z)$. The minor-axis velocity dispersion profiles are insensitive to inclinations and the parameter k that describes the partition of the mean-square azimuthal velocity $\overline{v_\phi^2}$ into random and mean components. Therefore, we have selected Υ for each galaxy to optimize the agreement between observation and the minor-axis velocity dispersion profile expected in the case of $i = 90°$ and an everywhere isotropic velocity ellipsoid ($k = 1$). The minor-axis dispersion profile is strictly indepenent of k and decreases slightly as i is lowered below 90°.

Decreasing the inclination also lowers slightly the major-axis dispersion profile but significantly increases the rotation speeds near the major axis. The increase in rotation velocity needed to give the increased flattening win out against the decrease due to projection. Thus, as i is decreased, the predicted position of a given galaxy in the (ϵ, v/σ) plane moves upward, as the virial theorem predicts (e.g., Binney 1982).

When the parameter k is set equal to unity, the velocity ellipsoids are everywhere isotropic and the streaming motions are excessive in all three galaxies. Lowering k below unity lowers the major-axis rotation curve and increases the corresponding dispersion profile. Thus lowering k pushes the galaxy downward in the (ϵ, v/σ) plane, as Satoh (1980) has already demonstrated. Since lowering k raises the major-axis dispersion profile while leaving the minor-axis profile constant, it is possible to limit the possible values of k by comparing the major- and minor-axis dispersion profiles.

In the case of NGC 720 the range of k-values permitted by the dispersion profiles does not encompass a value anything like as small as that required to bring the model rotation velocity into agreement with observation. Consequently, the distribution function of NGC 720 must involve an integral in addition to E and L_z. The measured rotation curve of NGC 1052, by contrast, does not require a value of k that lies outside the range permitted by the velocity dispersion profiles. Indeed, a model with $i = 90°$, $k = 0.7$ gives a reasonable account of all five long-slit measurements of NGC 1052. The case of NGC 4697, the galaxy studied by Satoh (1980) is intermediate between those of NGCs 720 and 1052: a model with $i = 90°$ and $k = 0.7$ fits the principal-axis profiles reasonably well. However, the streaming velocities predicted by this model away from the principal axes are consistently too large. Changing to an inclination $i < 90°$ would generate a conflict between the principal-axis profiles. Including a disk such as NGC 4697 has been suspected of harboring exacerbates the difficulties all round. Therefore, we conclude that NGC 4697, like NGC 720, probably does not have a distribution function of the form $f(E, L_z)$, although this conclusion is based on significantly weaker evidence than in the case of NGC 720. On the basis of less extensive data and simpler models Satoh concluded that NGC 4697 *could* have a distribution function of the form $f(E, L_z)$.

The minor-axis velocity dispersion profiles suggest that the mass-to-light ratio Υ is constant through the spectroscopically studied regions of these galaxies. The observed and predicted major-axis profiles of NGCs 720 and 1052 do differ in the way expected if Υ increased outward, but these discrepancies may equally arise from dependence of the distribution functions on a third integral.

This work demonstrates the necessity of proceeding to models with general distribution finctions $f(E, L_z, I_3)$. In such models there are two independent principal velocity dispersions in the meridional plane, which reduce in that plane to σ_R and σ_z. By exalting σ_R above σ_z the galaxy can be flattened without causing either σ_ϕ or $\overline{v_\phi}$ to become large. When we view such a model along the minor axis the line-of-sight dispersion comprises principally σ_R, while along the major axis we see predominantly σ_ϕ. Thus, flattening a galaxy with I_3 pushes the minor-axis dispersions up in relation to the major-axis dispersions, and *vice versa*, if we try, as in this paper, to flatten the system by exalting σ_ϕ. Figures 7 and 9 show that NGC 720 must be flattened by I_3, while NGC 1052 cannot have a distribution function that depends strongly on I_3. It is interesting to note that other data suggest that NGC 1052 is probably

triaxial (primarily the orientation of the gas rotation axis and the nonzero stellar minor axis rotation; see Davies and Illingworth 1986).

Much of the machinery employed here can be carried over without amendment to models with distribution functions of the form $f(E, L_z, I_3)$; all that needs to be upgraded is the derivation of σ and v_ϕ^2 from the Jeans equations. It is nontheless a nontrivial task to do this thoroughly. Let us hope that it will be accomplished before too long.

Frances Verter provided the initial stimulus from which this paper grew and did some pioneering work on the application of Lucy's method to deprojection of axisymmetric bodies. J. J. B. is grateful to the Institute for Advanced Study, Princeton, and Steward Observatory for their hospitality while this work, which at Princeton was supported by grant NAS5-29225, was underway. We are grateful to Roeland van der Marel for uncovering an error in the photometric constants used in an early version of the paper.

APPENDIX A

DENSITIES OF AXISYMMETRIC BODIES

Lucy (1974) gives a stable method for the recovery of a nonnegative theoretical distribution $T(\xi)$ from its projection $O(q) = \int K(q\,|\,\xi)T(\xi)d\xi$. The theoretical and observational coordinates ξ and q may, in general, be vectors of any dimension. The projection kernel K must satisfy the probability-like normalization $\int K(q\,|\,\xi)dq = 1$.

Let (X, Y, Z) be a system of Cartesian coordinates with the Z-axis parallel to the galaxy's symmetry axis, and the X-axis parallel to the line of nodes. Then if $R \equiv (X^2 + Y^2)^{1/2}$, the luminosity density is $l(R, Z)$. The first step in casting our problem into Lucy's form is to rewrite the line-of-sight integral of $l(R, Z)$ as an integral over the space spanned[3] by R^2 and Z. Since $l(R, Z) = \iint l(R', Z')\delta(R^2 - R'^2)\delta(Z - Z')dR'^2\,dZ'$, the surface brightness may be written

$$I(x, y) = \int_{-\infty}^{\infty} dz \int_0^{\infty} dR'^2 \delta[R^2(x, y, z) - R'^2] \int_{-\infty}^{\infty} dZ' l(R', Z')\delta[Z(x, y, z) - Z'] , \tag{11}$$

where (x, y, z) are Cartesian coordinates such that $x = X$ and the z-axis is parallel to the line of sight. If i is the galaxy's inclination, we have

$$\begin{aligned} Y &= y \cos i - z \sin i , \\ Z &= y \sin i + z \cos i . \end{aligned} \tag{12}$$

Substituting these expressions into equation (11), interchanging orders of integration, and integrating over z, we find

$$\begin{aligned} I(x, y) &= \int_0^{\infty} dR'^2 \int_{-\infty}^{\infty} dZ'\, l(R', Z') \frac{\delta\{[y \cos i - (Z' - y \sin i) \tan i]^2 - (R'^2 - x^2)\}}{|\cos i|} \\ &= \pi \int_0^{\infty} dR'^2 \int_{-\infty}^{\infty} dZ'\, l(R', Z') \frac{\delta[(y \sec i - Z' \tan i)^2 - (R'^2 - x^2)]}{\pi \cos i} . \end{aligned} \tag{13}$$

This expression casts the problem into the desired form: It is straightforward to check that the kernel

$$K(x, y\,|\,R, Z) \equiv \frac{\delta[(y \sec i - Z \tan i)^2 - (R^2 - x^2)]}{\pi \cos i} \tag{14a}$$

has the normalization

$$\int_{-\infty}^{\infty} dx \int_{-\infty}^{\infty} dy\, K(x, y\,|\,R, Z) = 1 . \tag{14b}$$

If the nth estimated distribution $j_n(R, Z)$ gives rise to the predicted observable $I_n(x, y)$, then in Lucy's method, the $(n + 1)$th estimate is

$$j_{n+1}(R, Z) = j_n(R, Z) \int_{-\infty}^{\infty} dx \int_{\infty}^{\infty} dy\, f_n(x, y)K(x, y\,|\,R, Z) , \tag{15a}$$

where

$$f_n \equiv \frac{I_{\rm obs}}{I_n} . \tag{15b}$$

Substituting equation (14a) into equation (15a) and integrating out y, we obtain

$$j_{n+1}(R, Z) = j_n(R, Z) \int_{-R}^{R} \sum_{\pm} f_n(x, y_{\pm}) \frac{dx}{2\pi\sqrt{R^2 - x^2}} . \tag{16a}$$

[3] The use of R^2 as a variable rather than R is a matter of pure convenience in the handling of δ-functions. However, written in terms of R^2, the integrals have a natural physical interpretation. We shall twice use the identity $\int f(x)\delta[g(x)]dx = \sum_{x_i} f(x_i)/|g'(x_i)|$, where x_i are the points at which $g(x) = 0$.

In this expression $y_\pm$ is a function of x, R, and Z through

$$y_\pm = Z \sin i \pm \sqrt{R^2 - x^2} \cos i \,. \tag{16b}$$

This is the equation of the ellipse on the sky to which the circle of constant R and Z projects. Changing to a new variable of integration ϕ for which $x = R \cos \phi$, equation (16a) becomes

$$j_{n+1}(R, Z) = j_n(R, Z) \int_{-\pi/2}^{\pi/2} f_n(R \cos \phi, Z \sin i + R \sin \phi \cos i) \frac{d\phi}{\pi} \,. \tag{17}$$

The function f_n is obtained from equations (15b) and (13), which becomes, on integrating out Z' and substituting $R' = x \cosh \psi$,

$$\begin{aligned} I_n(x, y) &= \frac{1}{\sin i} \int_0^\infty \sum_\pm j_n(R', y \csc i \pm x \sinh \psi \cot i) R' \, d\psi \qquad (x \neq 0) \,, \\ &= \frac{1}{\sin i} \int_0^\infty \sum_\pm j_n(R', y \csc i \pm R' \cot i) dR' \qquad (x = 0) \,. \end{aligned} \tag{18}$$

a) Interpolation Scheme

Fast accurate evaluation of the integrals involved in Lucy's deconvolution algorithm, and in the determination of the projected kinematic quantities, requires an effective scheme for two-dimensional interpolation. Let (a, θ) be elliptical coordinates related to Cartesian coordinates by $x = a \cos \theta$, $y = qa \sin \theta$. Then the functions to be handled are always even functions of θ and are either symmetric or antisymmetric about $\theta = \pi/2$. If f_{nm} are the values of the function $f(a, \theta)$ on the grid points $[(a_n, \theta_m); (n = 1, N), (m = 1, M)]$, then we first choose coefficients g_{nm} such that for all (n, m)

$$\begin{aligned} f(a_n, \theta_m) &= \sum_{m=1}^{M} g_{nm} \cos [2(m - 1)\theta_m] \,, \qquad \left(f \text{ symmetric about } \theta = \frac{\pi}{2}\right) ; \\ f(a_n, \theta_m) &= \sum_{m=1}^{M} g_{nm} \cos [(2m - 1)\theta_m] \,, \qquad \left(f \text{ antisymmetric about } \theta = \frac{\pi}{2}\right) . \end{aligned} \tag{19}$$

The estimated value of a function symmetric about $\theta = \pi/2$ is then

$$f(a, \theta) = \sum_{m=1}^{M} g_m(a) \cos [2(m - 1)\theta] \,, \tag{20}$$

where for each m, $g_m(a)$ is obtained by a cubic spline fit in log a to the g_{nm}. This scheme enables accurate interpolation of surface brightness, volume emissivities, and velocities for even small values of M.

APPENDIX B

VELOCITY AND VELOCITY DISPERSION DATA

The velocity and velocity dispersion data for each slit position are given in Tables, 3, 4, and 5 for NGC 720, 1052, and 4697, respectively. The radii r are in arcseconds from the center, with negative radii lying to the *east* of the nucleus or symmetry point. Radii enclosed by parenthesis are uncertain due to the effects of seeing and the positioning of the slit. The velocities V and velocity dispersions σ, and their asscoiated errors $\epsilon(V)$, $\epsilon(\sigma)$, are given in kilometers per second. The "line strength" γ is a scale factor for the fitted Gaussian velocity dispersion and is strongly affected in these data by scattered light in the image intensifier. As demonstrated elsewhere (e.g., Kormendy and Illingworth 1983), this has minimal effect on the measured dispersions but renders the line strength parameter of little use for quantitative analyses.

TABLE 3

ROTATION AND DISPERSION

r	$V(r)$	$\epsilon(V)$	$\sigma(r)$	$\epsilon(\sigma)$	$\gamma(r)$	$\epsilon(\gamma)$	r	$V(r)$	$\epsilon(V)$	$\sigma(r)$	$\epsilon(\sigma)$	$\gamma(r)$	$\epsilon(\gamma)$
NGC 720 Major Axis (P.A. = 143°)													
53.″2.....	116	29	184	33	0.53	0.06	−4.9.....	−32	9	234	11	0.81	0.04
38.7.....	54	13	148	17	0.49	0.03	−7.6.....	−22	8	223	8	0.78	0.03
28.7.....	63	13	201	14	0.55	0.03	−10.9.....	−27	8	205	7	0.67	0.02
22.3.....	28	12	190	13	0.53	0.03	−15.7.....	−53	8	224	8	0.66	0.02
16.2.....	29	8	206	8	0.61	0.03	−21.1.....	−45	12	223	12	0.62	0.03
11.7.....	33	10	213	10	0.65	0.03	−27.6.....	−37	10	196	11	0.58	0.03
8.5.....	39	11	234	10	0.74	0.03	−37.2.....	−99	14	192	15	0.53	0.03
5.2.....	33	9	236	8	0.81	0.03	−52.3.....	−86	29	207	36	0.47	0.06
NGC 720 Minor Axis (P.A. = 53°)													
−28.3.....	28	18	197	20	0.48	0.03	(1.0)....	43	13	271	12	1.01	0.04
−21.0.....	33	17	211	16	0.75	0.04	(2.3)....	30	11	247	10	0.93	0.04
−15.6.....	−20	13	229	12	0.69	0.03	4.3.....	12	10	249	9	0.87	0.03
−10.9.....	−8	9	210	8	0.71	0.02	7.6.....	−5	7	225	6	0.75	0.02
−6.5.....	−10	7	240	6	0.77	0.02	11.9.....	9	11	211	11	0.62	0.02
−3.3.....	21	12	241	11	0.85	0.03	16.5.....	−19	13	214	14	0.61	0.03
(−1.4)....	1	10	242	9	0.96	0.03	21.9.....	−6	17	176	19	0.56	0.04
(−0.7)....	20	12	266	11	1.02	0.04	28.4.....	−4	27	214	29	0.43	0.04
NGC 720 30° (P.A. = 113°)[a]													
53.2.....	26	16	165	20	0.47	0.03	(−0.7)....	20	12	235	12	0.84	0.04
38.8.....	33	16	185	21	0.45	0.03	(−1.4)....	12	12	237	12	0.84	0.04
28.8.....	43	9	185	10	0.54	0.02	(−3.3)....	4	11	228	11	0.79	0.03
18.5.....	36	6	190	6	0.61	0.01	−6.6.....	−15	6	220	6	0.81	0.02
11.9.....	13	8	225	7	0.76	0.02	−10.9.....	−29	8	218	8	0.74	0.02
7.8.....	18	6	212	6	0.76	0.02	−17.6.....	−42	6	227	6	0.67	0.02
4.3.....	−1	12	251	11	0.85	0.03	−27.1.....	−21	10	208	10	0.58	0.02
(2.4)....	−1	13	270	11	0.90	0.04	−37.2.....	−21	12	152	15	0.47	0.02
(1.0)....	−11	13	229	14	0.84	0.04	−49.8.....	−44	13	143	19	0.48	0.03

NOTE.—Values given in second through fifth columns are in km s^{-1}. Parentheses around radius values indicate radius uncertain; actual radius depends upon seeing and positioning of slit with respect to nucleus.

Radii to the *east* of the nucleus or symmetry point are *negative*.

[a] 30° from the major axis.

TABLE 4

ROTATION AND DISPERSION DATA

r	$V(r)$	$\epsilon(V)$	$\sigma(r)$	$\epsilon(\sigma)$	$\gamma(r)$	$\epsilon(\gamma)$	r	$V(r)$	$\epsilon(V)$	$\sigma(r)$	$\epsilon(\sigma)$	$\gamma(r)$	$\epsilon(\gamma)$
NGC 1052 Major Axis (P.A. = 117°)													
45.″3.....	69	16	132	24	0.52	0.05	(−1.0)....	−37	16	225	19	1.01	0.07
36.5.....	101	18	211	23	0.84	0.06	(−1.5)....	−51	13	227	10	0.97	0.04
33.0.....	98	15	186	19	0.72	0.05	−2.6.....	−59	13	220	16	0.91	0.05
28.6.....	105	13	176	17	0.68	0.04	−3.3.....	−63	8	206	8	0.94	0.03
24.7.....	116	10	189	13	0.68	0.04	4.7.....	−52	9	196	9	0.90	0.03
21.3.....	117	12	188	15	0.74	0.04	−5.4.....	−66	10	203	11	0.87	0.04
18.7.....	101	9	174	12	0.78	0.04	−7.2.....	−78	6	197	7	0.81	0.02
15.8.....	84	8	188	9	0.77	0.03	−9.1.....	−79	9	190	11	0.77	0.03
12.8.....	81	8	176	10	0.75	0.03	−10.8.....	−89	7	183	8	0.76	0.02
10.7.....	73	7	194	8	0.83	0.02	−13.9.....	−76	7	182	8	0.76	0.02
8.4.....	73	7	187	8	0.82	0.02	−16.2.....	−101	10	200	13	0.73	0.04
6.9.....	67	8	189	10	0.83	0.03	−19.3.....	−92	8	203	10	0.73	0.03
5.9.....	59	8	184	9	0.88	0.03	−22.1.....	−87	15	175	18	0.64	0.05
4.7.....	50	10	207	12	0.89	0.04	−24.8.....	−82	13	206	16	0.71	0.04
4.0.....	72	9	210	9	0.98	0.03	−28.6.....	−120	11	180	14	0.70	0.04
(2.4)....	65	8	205	8	0.93	0.03	−33.5.....	−108	22	193	27	0.77	0.07
(1.7)....	48	15	218	18	0.95	0.06	−37.5.....	−88	30	186	38	0.67	0.09
(1.0)....	37	13	...	...	...	...	−45.2.....	−96	16	184	21	0.69	0.05
(0.7)....	9	16	250	11	1.03	0.05							

TABLE 4—*Continued*

r	$V(r)$	$\epsilon(V)$	$\sigma(r)$	$\epsilon(\sigma)$	$\gamma(r)$	$\epsilon(\gamma)$	r	$V(r)$	$\epsilon(V)$	$\sigma(r)$	$\epsilon(\sigma)$	$\gamma(r)$	$\epsilon(\gamma)$
NGC 1052 Minor Axis (P.A. = 28°)													
28.3.....	−2	39	126	62	0.75	0.16	(−1.5)....	−5	11	242	11	0.98	0.04
23.3.....	7	23	165	28	0.82	0.08	−2.9.....	−1	8	219	9	0.92	0.03
19.2.....	−3	14	173	18	0.85	0.05	−4.6.....	−3	8	176	9	0.82	0.03
15.5.....	28	12	156	16	0.73	0.04	−5.5.....	−5	14	199	18	0.81	0.05
12.8.....	18	16	187	20	0.82	0.06	−7.2.....	10	10	187	11	0.75	0.03
10.6.....	27	11	193	13	0.75	0.03	−9.0.....	−10	15	192	19	0.86	0.06
8.1.....	7	11	218	11	0.85	0.03	−10.8.....	−20	11	194	13	0.78	0.03
6.0.....	4	9	174	11	0.83	0.03	−13.7.....	−7	16	177	21	0.79	0.06
4.1.....	−3	9	206	9	0.94	0.03	−15.5.....	−19	14	164	18	0.59	0.04
(2.3)....	−9	7	206	8	0.96	0.03	−19.6.....	−11	15	175	18	0.65	0.04
(1.7)....	6	15	222	19	0.98	0.06	−24.0.....	−9	24	189	25	0.68	0.06
(0.6)....	11	8	229	9	1.03	0.04	−29.6.....	−42	27	167	28	0.73	0.07
(−0.9)....	3	17	208	21	1.02	0.07							
NGC 1052 45° Ray Pg[a] (P.A. = 73°)													
13.8.....	...	...	211	12	0.73	0.04	(−0.9)....	...	...	235	7	1.04	0.04
6.7.....	...	...	166	9	0.77	0.02	−3.8.....	...	...	219	8	0.88	0.03
4.0.....	...	...	214	9	0.90	0.03	7.1.....	...	...	192	12	0.75	0.03
(2.2)....	...	...	217	9	0.99	0.04	−13.5.....	...	...	176	11	0.65	0.03
NGC 1052 45° Ray (P.A. = 73°/163°)													
39.8.....	38	14	153	22	0.74	0.05	(−1.0)....	−55	10	227	11	0.98	0.05
32.0.....	51	16	169	23	0.68	0.05	(−1.7)....	−54	9	227	9	0.98	0.04
27.6.....	55	13	157	19	0.79	0.05	−2.5.....	−53	8	226	9	0.98	0.04
23.6.....	25	13	173	21	0.65	0.04	−3.5.....	−34	9	213	11	0.88	0.04
19.1.....	48	8	173	12	0.83	0.03	−4.5.....	−35	8	215	9	0.89	0.03
16.1.....	38	9	176	13	0.81	0.04	−5.7.....	−46	9	201	11	0.87	0.03
13.3.....	39	7	187	9	0.89	0.03	−7.0.....	−50	7	201	9	0.86	0.03
10.8.....	51	8	194	11	0.89	0.04	−8.9.....	−39	6	204	8	0.88	0.03
8.9.....	40	6	206	8	0.91	0.03	−11.1.....	−40	8	195	10	0.89	0.03
6.7.....	42	7	205	9	0.89	0.03	−13.6.....	−25	7	177	10	0.83	0.03
5.7.....	41	12	205	16	0.93	0.06	−16.3.....	−48	9	184	12	0.84	0.03
4.6.....	32	6	216	8	0.94	0.03	−20.1.....	−52	10	204	15	0.85	0.03
3.3.....	27	10	216	11	1.01	0.05	−24.5.....	−43	13	199	16	0.79	0.04
2.6.....	32	7	228	8	0.99	0.04	−28.5.....	−32	23	163	32	0.67	0.07
(1.7)....	17	8	239	9	1.05	0.04	−32.3.....	−38	18	186	25	0.69	0.06
(1.0)....	0	9	235	9	1.05	0.04	−40.3.....	−37	25	208	31	0.73	0.08
(0.7)....	−24	10	230	10	0.99	0.05							
NGC 1052 Offset SW 13″ Parallel (P.A. = 115°)													
41.7.....	89	16	155	19	0.57	0.04	(−0.7)....	25	13	197	12	0.82	0.04
31.7.....	86	12	174	13	0.69	0.03	(−1.4)....	2	12	189	11	0.81	0.03
25.1.....	72	12	153	14	0.66	0.03	−3.9.....	−8	8	174	8	0.78	0.02
20.6.....	79	11	132	13	0.59	0.03	−7.2.....	−29	11	173	12	0.70	0.03
15.6.....	40	10	173	10	0.72	0.03	−10.3.....	−56	11	178	12	0.67	0.03
11.2.....	18	9	170	10	0.74	0.03	−14.7.....	−57	11	176	10	0.69	0.03
8.1.....	9	10	179	11	0.74	0.03	−19.7.....	−74	12	168	14	0.69	0.04
5.9.....	31	10	161	11	0.78	0.03	−24.2.....	−64	12	134	16	0.61	0.04
4.0.....	9	9	164	10	0.80	0.03	−30.1.....	−77	11	135	13	0.60	0.03
(2.3)....	−3	10	162	11	0.79	0.03	−42.4.....	−31	14	167	17	0.63	0.04
(1.0)....	−11	12	177	13	0.75	0.04							
NGC 1052 Offset SE 15″ Perpendicular (P.A. = 29°)													
−25.4.....	−23	15	204	17	0.60	0.04	(1.0)....	−98	10	149	11	0.73	0.03
−19.7.....	−29	12	158	14	0.71	0.04	(2.3)....	−85	9	170	10	0.72	0.03
−14.7.....	−40	11	200	11	0.82	0.04	5.1.....	−60	6	161	6	0.78	0.02
−10.3.....	−65	8	169	9	0.80	0.03	8.1.....	−59	9	165	9	0.74	0.03
−7.2.....	−69	10	193	10	0.74	0.03	11.2.....	−51	10	168	10	0.70	0.03
−4.9.....	−78	9	166	10	0.72	0.03	15.6.....	−44	11	186	11	0.71	0.03
−3.1.....	−63	9	159	10	0.69	0.03	20.6.....	−48	12	155	15	0.69	0.04
(−1.4)....	−80	8	166	8	0.80	0.03	27.3.....	−14	13	170	17	0.59	0.04
(−0.7)....	−100	9	149	10	0.77	0.03							

NOTES.—Radii to the *east* of the nucleus or symmetry point are *negative*. Data given in second through fifth are in units of km s^{-1}. Parentheses around radius values indicate radius uncertain; actual radius depends upon seeing and positioning of slit with respect to nucleus.

[a] High-resolution photographic data used to confirm that Cryogenic Camera data (in particular that in PA 73° and PA 164°) has the same $\sigma(r)$ zero point to within 5%.

TABLE 5

ROTATION AND DISPERSION DATA

r	$V(r)$	$\epsilon(V)$	$\sigma(r)$	$\epsilon(\sigma)$	$\gamma(r)$	$\epsilon(\gamma)$	r	$V(r)$	$\epsilon(V)$	$\sigma(r)$	$\epsilon(\sigma)$	$\gamma(r)$	$\epsilon(\gamma)$
NGC 4697 Major Axis (P.A. = 63°)													
66″.0	97	12	129	18	0.36	0.02	(−0.7)	−14	11	...	...	...	...
52.9	99	10	146	13	0.44	0.02	(−1.4)	−27	8	174	8	0.72	0.02
43.4	101	8	159	10	0.51	0.02	(−3.9)	−77	9	178	7	0.70	0.02
34.0	105	7	169	8	0.51	0.02	(−5.6)	−76	8	...	...	...	...
24.3	103	5	159	6	0.52	0.01	−7.8	−76	6	170	6	0.66	0.02
16.9	81	6	176	7	0.56	0.02	−11.6	−79	5	178	6	0.63	0.02
12.1	75	5	163	6	0.55	0.02	−16.3	−104	6	168	6	0.59	0.02
8.2	76	6	179	5	0.68	0.01	−23.3	−96	5	169	5	0.59	0.01
6.2	87	7	...	...	...	...	−33.1	−97	6	168	7	0.55	0.02
4.3	79	10	175	9	0.64	0.02	−43.9	−113	7	173	8	0.52	0.02
(2.3)	40	11	...	...	...	...	−55.0	−125	13	149	18	0.41	0.03
(1.0)	−1	10	187	8	0.66	0.02	−65.1	−115	13	144	17	0.44	0.03
NGC 4697 Minor Axis (P.A. = 153°)													
−58.6	−19	36	218	32	0.49	0.06	(2.3)	16	11	...	...	...	...
−44.1	−10	11	176	12	0.63	0.03	4.1	−11	9	174	9	0.72	0.03
−32.9	−10	9	183	11	0.61	0.03	5.8	15	7	190	7	0.71	0.02
−23.5	3	7	183	7	0.60	0.02	8.2	4	7	197	7	0.71	0.02
−15.9	3	8	185	8	0.56	0.02	11.5	−4	7	174	8	0.58	0.02
−11.2	9	7	189	7	0.65	0.02	16.2	4	7	169	8	0.60	0.02
−7.9	−5	7	173	7	0.68	0.02	23.8	−7	8	195	9	0.53	0.02
−5.7	−10	7	182	7	0.74	0.02	33.2	−2	10	163	12	0.51	0.02
−3.7	0	8	187	8	0.78	0.03	43.4	−21	14	178	19	0.44	0.03
(−1.4)	8	11	...	...	...	...	55.2	27	17	150	23	0.45	0.04
(−0.7)	2	9	...	...	...	...							
NGC 4697 Offset NW 10″ Parallel (P.A. = 63°)													
57.2	76	11	144	14	0.41	0.02	(−0.7)	−20	11	174	12	0.83	0.04
43.2	87	11	161	13	0.58	0.03	(−1.4)	−2	11	160	12	0.73	0.04
33.9	77	8	165	10	0.66	0.03	−3.4	−5	11	173	12	0.73	0.04
24.5	40	8	179	8	0.73	0.03	6.5	−10	8	159	9	0.68	0.03
16.7	48	11	174	12	0.69	0.04	−11.0	−38	10	168	11	0.74	0.04
12.0	27	10	164	11	0.76	0.04	−15.7	−52	9	176	10	0.77	0.04
7.6	14	7	170	8	0.79	0.03	−23.4	−48	7	153	9	0.64	0.03
4.3	−6	10	158	11	0.73	0.04	−33.1	−63	9	175	10	0.68	0.03
(2.4)	10	9	154	10	0.81	0.04	−44.4	−78	10	142	12	0.49	0.03
(1.0)	5	11	154	13	0.78	0.04	−58.1	−117	15	134	21	0.45	0.04
NGC 4697 Offset SE 20″ Parallel (P.A. = 63°)													
68.8	−24	15	138	21	0.38	0.04	−7.7	−3	18	178	21	0.57	0.05
47.0	29	10	133	14	0.48	0.03	−11.0	−25	16	170	22	0.62	0.06
33.1	31	13	157	16	0.54	0.04	−15.8	−18	12	184	14	0.72	0.05
24.3	32	10	162	12	0.60	0.04	−24.1	−20	10	143	13	0.60	0.04
16.8	25	12	171	14	0.68	0.05	−32.7	−36	13	161	16	0.55	0.04
10.5	29	11	167	12	0.64	0.04	−46.9	−52	10	161	13	0.58	0.03
6.2	10	20	171	23	0.59	0.06	−77.3	−77	12	105	18	0.35	0.03
4.3	49	17	172	20	0.65	0.06							
NGC 4697 Offset[a] 22″ Perpendicular (PA 153°)													
−61.2	−37	19	187	27	0.86	0.08	(1.0)	79	8	176	10	0.91	0.04
−44.5	−9	9	187	12	0.78	0.03	(2.4)	90	9	199	9	0.92	0.04
−33.1	39	8	179	11	0.81	0.03	4.3	76	9	157	12	0.69	0.03
−23.1	22	6	173	8	0.84	0.03	7.6	54	6	177	7	0.90	0.03
−15.7	30	7	172	9	0.83	0.03	11.9	37	9	184	11	0.85	0.04
−11.0	49	10	164	13	0.65	0.03	16.6	30	9	161	11	0.76	0.04
6.5	65	6	173	8	0.79	0.03	24.4	37	8	179	10	0.74	0.03
−3.4	86	8	202	9	1.00	0.04	33.8	37	9	188	12	0.75	0.03
(−1.4)	110	8	189	10	0.89	0.04	43.8	18	10	167	14	0.78	0.04
(−0.7)	95	10	188	13	0.85	0.04	51.8	−4	21	192	32	0.56	0.05

NOTES.—Radii to the *east* of the nucleus or symmetry point are *negative*. Data given in cols. (2)–(5) are in units of km s^{-1}. Parentheses around radius values indicate radius uncertain; actual radius depends upon seeing and positioning of slit with respect to nucleus.

[a] Average of two spectra, both offset and parallel to minor axis. One offset 22″ to NE along major axis, other offset 22″ SW.

REFERENCES

Allen, C. W. 1973, *Astrophysical Quantities* (3rd ed.; London: Athlone).
Bertola, F., and Capaccioli, M. 1975, *A.J.*, **200**, 439.
Bessell, M. S. 1979, *Pub. A.S.P.*, **91**, 589.
Binney, J. J. 1976, *M.N.R.A.S.*, **177**, 19.
———. 1978, *M.N.R.A.S.*, **183**, 501.
———. 1982, in *Morphology and Dynamics of Galaxies, 12th Adv. Course Swiss Soc. Astr. Ap.*, ed. L. Martinet and M. Mayor (Sauverny: Geneva Observatory), p. 3.
Binney, J. J., and Mamon, G. A. 1982, *M.N.R.A.S.*, **200**, 361.
Binney, J. J., and Petit, J.-M. 1988, in *Dense Stellar Systems*, ed. D. Merritt (Cambridge: Cambridge University Press), p. 43.
Burstein, D., Davies, R. L., Dressler, A., Faber, S. M., Stone, R. P. S., Lynden-Bell, D., Terlevich, R., and Wegner, G. 1987, *Ap. J. Suppl.*, **64**, 601.
Canizares, C. R., Fabbiano, G., and Trinchieri, C. 1987, *Ap. J.*, **312**, 503.
Carter, D. 1987, *Ap. J.*, **312**, 514.
Davies, R. L., Burstein, D., Dressler, A., Faber, S. M., Lynden-Bell, D., Terlevich, R. J., and Wegner, G. 1987, *Ap. J. Suppl.*, **64**, 581.
Davies, R. L., and Illingworth, G. D. 1983, *Ap. J.*, **266**, 516.
———. 1986, *Ap. J.*, **302**, 234.
Davis, L. E., Cawson, M., Davies, R. L., and Illingworth, G. D. 1985, *A.J.*, **90**, 169.
Dejonghe, H. 1986, *Phys. Rept.*, **133**, 217.
de Vaucouleurs, G., de Vaucouleurs, A., and Corwin, H. G. 1976, *Second Reference Catalogue of Bright Galaxies* (Austin: University of Texas Monogr. Astr., No. 2) (RC2).
Dressler, A. 1979, *Ap. J.*, **231**, 659.
Dressler, A., and Richstone, D. O. 1988, *Ap. J.*, **324**, 701.
Dressler, A., Schechter, P. L., and Rose, J. A. 1986, *A.J.*, **91**, 1058.
Efstathiou, G., Ellis, R. S., and Carter, D. 1982, *M.N.R.A.S.*, **201**, 975.
Fillmore, J. A. 1986, *A.J.*, **91**, 1096.
Freeman, K. C. 1970, *Ap. J.*, **160**, 811.
Hunter, C. 1975, *A.J.*, **80**, 783.
Illingworth, G. D. 1977, *Ap. J. (Letters)*, **218**, L43.
Illingworth, G. D., and Schechter, P. L. 1982, *Ap. J.*, **256**, 481.
Jaffe, W. 1983, *M.N.R.A.S.*, **202**, 995.
Jarvis, B. J., and Freeman, K. C. 1985, *Ap. J.*, **295**, 324.
Jedrzejewski, R. I., Davies, R. L., and Illingworth, G. D. 1987, *A.J.*, **94**, 1508.
Knapp, G. R., Guhathakurta, P., Kim, D.-W., and Jura, M. 1988, *Ap. J. Suppl.*, **70**, 329.
Kormendy, J., and Illingworth, G. D. 1983, *Ap. J.*, **265**, 632.
Lucy, L. B. 1974, *A.J.*, **79**, 745.
Lynden-Bell, D. 1962, *M.N.R.A.S.*, **123**, 447.
Merritt, D. 1987, *Ap. J.*, **319**, 55.
Newton, A. J. 1986, D. Phil thesis, Oxford University.
Peletier, R. F., Davies, R. L., Illingworth, G. D., Davis, L. E., and Cawson, M. 1990, *A.J.*, in press.
Prendergast, K. H., and Tomer, E. 1970, *A.J.*, **75**, 674.
Rood, H. J., Page, T. L., Kintner, E. C., and King, I. R. 1972, *Ap. J.*, **175**, 627.
Rowley, G. 1988, *Ap. J.*, **331**, 124.
Sandage, A., and Tammann, G. A. 1981, *A Revised Shapley Ames Catalogue of Bright Galaxies* (Washington, DC: Carnegie Institution of Washington) (RSA).
Sargent, W. L. W., Young, P. J., Boksenberg, A., Shortridge, K., Lynds, C. R., and Hartwick, F. D. A. 1978, *Ap. J.*, **221**, 731.
Satoh, C. 1980, *Publ. Astr. Soc. Japan*, **32**, 41.
Schechter, P. L. 1980, *A.J.*, **85**, 801.
Tonry, J. L. 1983, *Ap. J.*, **266**, 58.
———. 1984, *Ap. J. (Letters)*, **283**, L27.
Toomre, A. 1962, *Ap. J.*, **138**, 385.
van der Marel, R., Binney, J. J., and Davies, R. L. 1990, *M.N.R.A.S.*, in press.
Wilson, C. P. 1975, *A.J.*, **80**, 175.

J. J. BINNEY: Department of Theoretical Physics, Keble Road, Oxford OX1 3NP, England, UK

ROGER L. DAVIES: Department of Astrophysics, Keble Road, Oxford OX1 3RH, England, UK

GARTH D. ILLINGWORTH: Lick Observatory, University of California, Santa Cruz, CA 95064